A&A 587, A135 (2016)
DOI: 10.1051/0004-6361/201424484

Astronomy & Astrophysics

NGC 6334 and NGC 6357: Hα kinematics and the nature of the H II regions⋆

D. Russeil[1], J. Tigé[1], C. Adami[1], L. D. Anderson[2,3], N. Schneider[4,5], A. Zavagno[1], M. R. Samal[1], P. Amram[1], L. Guennou[6,1], E. Le Coarer[7], A. Walsh[8], S. N. Longmore[9], and C. Purcell[10]

[1] Aix Marseille Université, CNRS, LAM (Laboratoire d'Astrophysique de Marseille), UMR 7326, 13388 Marseille, France
e-mail: delphine.russeil@lam.fr
[2] Department of Physics and Astronomy, West Virginia University, Morgantown, West Virginia, WV 26506, USA
[3] Adjunct Astronomer at the National Radio Astronomy Observatory, PO Box 2, Green Bank, WV 24944, USA
[4] LAB/OASU, UMR 5804, CNRS, Université de Bordeaux, 33270 Floirac, France
[5] I. Physik. Institut, University of Cologne, 50931 Cologne, Germany
[6] IAS, CNRS & Université Paris Sud, Bâtiment 121, 91405 Orsay, France
[7] Laboratoire d'Astrophysique de Grenoble, Université Joseph Fourier, CNRS, BP 53, 38041 Grenoble Cedex, France
[8] International Centre for Radio Astronomy Research, Curtin University, GPO Box U1987, Perth, WA 6845, Australia
[9] European Southern Observatory, Karl-Schwarzschild-Str. 2, 85748 Garching, Germany
[10] School of Physics and Astronomy, University of Leeds, Leeds, LS2 9JT, UK

Received 27 June 2014 / Accepted 18 December 2015

ABSTRACT

Aims. NGC 6334 and NGC 6357 are amongst the most active, optically visible Galactic star-forming complexes. They are composed of several H II regions that have a significant impact on their surrounding. The aim of this paper is to present a kinematic study of the optical H II regions that belong to NGC 6334 and NGC 6357.
Methods. We use Fabry-Perot interferometer observations of the Hα line, which cover NGC 6334 and NGC 6357. These observations allow us to analyse the Hα line profiles to probe the kinematics of the ionised gas of both regions. We complement the Hα observations with multi-wavelength data to specify the nature of the H II regions.
Results. We determine the dynamical nature of the optical H II regions that belongs to NGC 6334 and NGC 6357. In NGC 6334, GUM 61 is an expanding wind shell-like H II region, GUM 64b exhibits a champagne flow, GM1-24 is the Hα counterpart of two larger regions and H II 351.2+0.5 is, in fact, composed of two H II regions. In NGC 6357, H II 353.08+0.28 and H II 353.09+0.63 are probably stellar wind-shaped bubble H II regions, while H II 353.42+0.45 is a classical photo-ionised H II region. We suggest that, at large scale, star-formation seems to be triggered where large/old H II regions intersect. Inversely, stellar formation seems to have already started in the NGC 6334 north-east filament, irrespective of any evident external H II region impact. While NGC 6357 shows more complicated kinematics, NGC 6334 is characterised by a more active stellar formation.

Key words. HII regions – ISM: individual objects: NGC 6334 – ISM: individual objects: NGC 6357 – ISM: kinematics and dynamics

1. Introduction

High-mass (O- or B-type) stars play a major role in the energy budget and enrichment of galaxies through the development of their H II regions. The study of the H II regions allows us to quantify the impact of massive stars on their environment (e.g. triggered star-formation, dispersion of the molecular surrounding material, formation of pillars). H II regions can be found isolated or grouped into very active star-formation complexes, which makes their impact on the local interstellar medium more or less significant. Deharveng et al. (2010) and Thompson et al. (2012) show that H II regions can display an accumulation of dense material at their edges and, sometimes, contain condensations in which subsequent star formation can occur (e.g. Brand et al. 2011). Observations made with *Herschel* confirm that H II regions can trigger the formation of stars on their edges (e.g. Zavagno et al. 2010a, b). During their evolution, H II regions display different aspects: from hyper/ultra compact (size <0.1 pc and electron density $n_e > 3000$ cm^{-3}), which is exclusively seen in radio, to classical evolved H II regions (size >1 pc and $n_e \sim 100$ to 1000 cm^{-3}), which are observable in Hα (when extinction is faint). When the expanding H II region breaks its natal molecular cloud it may form a "blister" H II region, which flows away like a "champagne flow" (see Tenorio-Tagle 1979). Sometimes, H II regions display bubble-like (or shell-like) morphology. This type of morphology appears when the stellar wind drives a shock inside the Stromgren sphere, forming a dense shell which can trap all the ionizing flux from the star (e.g. Comeròn 1997). On the other hand, Tremblin et al. (2012a,b), emphasise that the expansion of the ionized gas from a H II region into a molecular cloud, and the associated turbulence, are important parameters for the formation of dense continuous layers, as well as pillars and globules in the interaction zone.

To better understand the impact of H II regions on the local interstellar medium and on subsequent star formation, in this paper we present a study of the kinematics of the ionized gas in NGC 6334 and NGC 6357 star-forming complexes. Our goal is to clarify the nature (blister, shell-like or bow-shock H II region,

⋆ The Hα data (FITS cubes) are only available at the CDS via anonymous ftp to cdsarc.u-strasbg.fr (130.79.128.5) or via http://cdsarc.u-strasbg.fr/viz-bin/qcat?J/A+A/587/A135

supernova remnant etc.) of the radio and optical H II regions that belong to them.

2. General overview

A general overview of NGC 6334 and NGC 6357 is presented in Fig. 1 with the H II region catalogs of Langston et al. (2000) and Anderson et al. (2014) overlaid. The Langston et al. (2000) radio (at 8.35 GHz and 14.35 GHz) regions are mainly extended H II regions (with a size larger than 4′). Anderson et al. (2014), by combining radio and mid-infrared Wide-Field Infrared Survey Explorer (WISE) observations, produced a catalog[1] of H II regions and candidate H II regions down to a size of 0.2′. Several of these regions are common in both catalogs. In Table A.1, we provide the correspondance between them and we indicate if an associated Hα emission is observed on the AAO-UKST Hα image (Parker et al. 2005).

NGC 6334 (l = 351.2°, b = +0.7°) is a well studied region (as reviewed by Persi & Tapia 2008). At SIMBA-1.2 mm (Muñoz et al. 2007), the central part of NGC 6334 consists of a 10 pc long filament that is associated with large extinction (Russeil et al. 2010) and seen as a very intense molecular and dust ridge (e.g. Zernickel et al. 2012; Russeil et al. 2013). Optically, NGC 6334 is a grouping of the well-known optical H II regions GUM61, GUM 62, GUM 63, GUM 64, HII 351.2+0.5, and GM1-24 (Persi & Tapia 2008). GUM 61 appears as a particular region since its optical emission (see Fig. 5 in Carral et al. 2002) follows a quite regular filamentary lattice morphology. This kind of unusual filamentary structure in a circumstellar shell has been interpreted by van Marle & Keppens (2012) as instabilities that develop when massive star stellar winds collide with the circumstellar medium.

In Fig. 1 (upper panel) the optical H II regions have radio emission counterparts that allows us to follow their extension toward extinct area. Inversely, large radio emissions have no or a very faint Hα counterpart but they have their border clearly underlined by the 8 μm emission that traces PAH (Polycyclic Aromatic Hydrocarbon) while several compact radio sources have been noted with a strong 8 μm and/or 22 μm counterpart. The molecular emission associated with NGC 6334 has a mean velocity of −4 km s^{-1}, which is in agreement with the mean ionized gas velocity of ∼−3 km s^{-1} (Caswell & Haynes 1987).

NGC 6357 (l = 353.4°, b = +0.6°) is a large H II region, which exhibitis an annular morphology in the radio and optical (e.g. Lortet et al. 1984). The brightest H II region (G353.2+0.9) is a sharp boundary that faces the massive open cluster Pismis 24. In addition, four distinct optical H II regions can be noted (HII 353.42+0.45, HII 353.08+0.28, HII 353.09+0.63, and HII 353.24+0.60) with different morphology (Fig. 1, lower panel). Amid them HII 353.09+0.63 is clearly powered by the stellar cluster AH03J1725-34.4. The velocity of NGC 6357 is ∼−4 km s^{-1} (ionized gas, Caswell & Haynes 1987), which is similar to the mean velocity of NGC 6334 and strongly suggests that both regions are at the same distance. We adopt a distance of 1.75 kpc (see Lima et al. 2014; Persi et al. 2008; Russeil et al. 2010).

3. Observations and data

3.1. Hα data

Data cubes (x, y, λ) were obtained in 1994 with a 36 cm telescope located at ESO − La Silla Observatory, which was equipped with a scanning Fabry-Perot interferometer and a photon counting camera. The interference order of the Fabry-Perot interferometer used is 2604 at Hα wavelength, which provides a spectral sampling of 5 km s^{-1} for a spectral range of 115 km s^{-1} and a typical velocity accuracy of 1 km s^{-1} (le Coarer et al. 1992). The interference filter used is centred at 6562 Å, with a FWHM 11 Å.

Each data cube that was obtained has a pixel size of 9″ × 9″ and a field of view of 38′ × 38′. The spatial coverage of NGC 6334 and NGC 6357 requires six and eight fields respectively. Figures 2 and 3 show the mosaic of observed fields. The contrast of these figures has been adapted to underline the faint and diffuse emissions but a better view of the central high intensity areas can be seen in Figs. 10, 12, and 13.

A complete description of the instrument, including data acquisition and reduction techniques, can be found in le Coarer et al. (1992). Our data reduction follows the procedures described in Georgelin et al. (1994). The night-sky lines (geocoronal Hα and OH) are modelled by the instrumental function, the nebular lines being modelled by Gaussian profiles that have been convolved with the instrumental function. The Hα line profiles are complicated. This is illustrated by Fig. 4 where the two upper panels are typical Hα profiles from diffuse ionized hydrogen. Three nebular components around −5, −19, and +9 km s^{-1} are required to fit the profiles (in addition to the geocoronal Hα and OH nightsky lines) with each one corresponding to a different layer of ionized hydrogen that is present along the line of sight. Generally each component exhibits a similar velocity over the observed area, which enables us to follow it quite easily despite its highly varying intensity. As an example, in Fig. 4, the lower panel shows the profile integrated through 18″ × 18″ region in the central part of GUM 61. Because of the high intensity of the nebula, the profile is dominated by the nebular emissions with velocity −5 (component A), +24 (component B), and +41 km s^{-1} (component C), respectively. From this profile decomposition and following Rozas et al. (2006), one can estimate an expansion velocity of about ∼23 km s^{-1}, which is in agreement with Johnson (1982), who finds an expansion velocity of 18 km s^{-1}.

3.2. Ancillary data

We complement our Hα observations with the following public data:

3.2.1. SGPS and MGPS data

The Southern Galactic Plane Survey (SGPS)[2] is a survey of the 21 cm continuum and H I spectral line emission in the fourth quadrant and parts of the first and third quadrants of the disk of the Milky Way (McClure-Griffiths et al. 2005, Haverkorn, et al. 2006). The SGPS consists of two surveys: a low-resolution ($FWHM$ = 15′) survey that was completed with the Parkes 64 m radio telescope and a high-resolution ($FWHM$ = 2′) interferometric survey that was completed with the Australia Telescope Compact Array (ATCA). The data have been combined to provide a data set that has an angular resolution of about 2 arcmin, a spectral resolution of 0.82 km s^{-1}, and a sensitivity limit of ∼1.6 K in the line.

[1] http://astro.phys.wvu.edu/wise

[2] Data-cubes and images of NGC 6334 and NGC 6357 have been retrieved from http://www.atnf.csiro.au/research/HI/sgps/

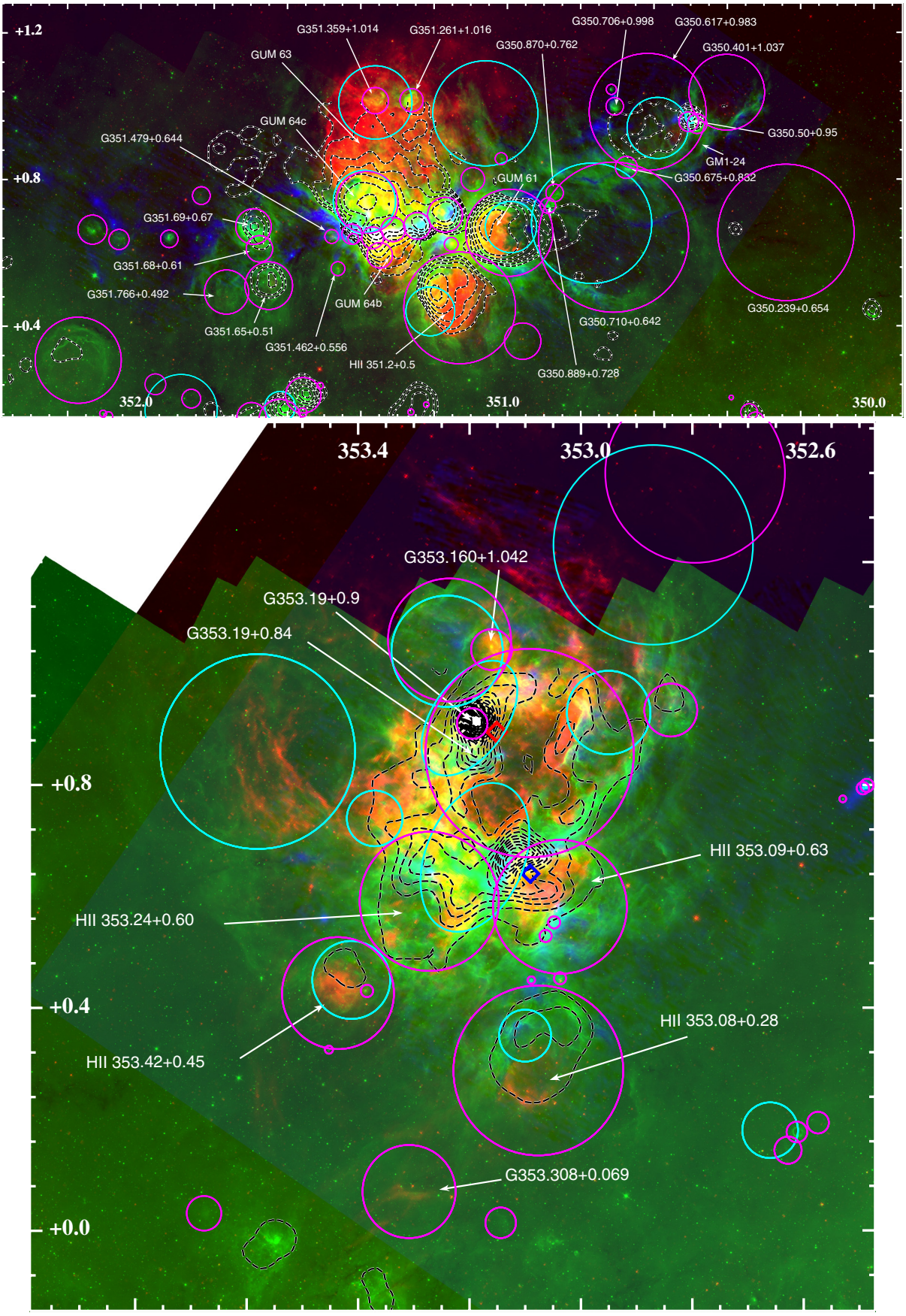

Fig. 1. Hα (red), GLIMPSE-8 μm (green), and SIMBA-1.2 mm (blue) composite image of NGC 6334 (*upper panel*) and NGC 6357 (*lower panel*). The quoted coordinates are galactic coordinates. The overlaid isocontours are from SGPS radio emission. The purple and cyan circles show the H II regions from Anderson et al. (2014) and Langston et al. (2000) respectively. For NGC 6357, the position of stellar clusters Pismis 24 (red diamond) and AH03J1725-34.4 (blue diamond) are also indicated.

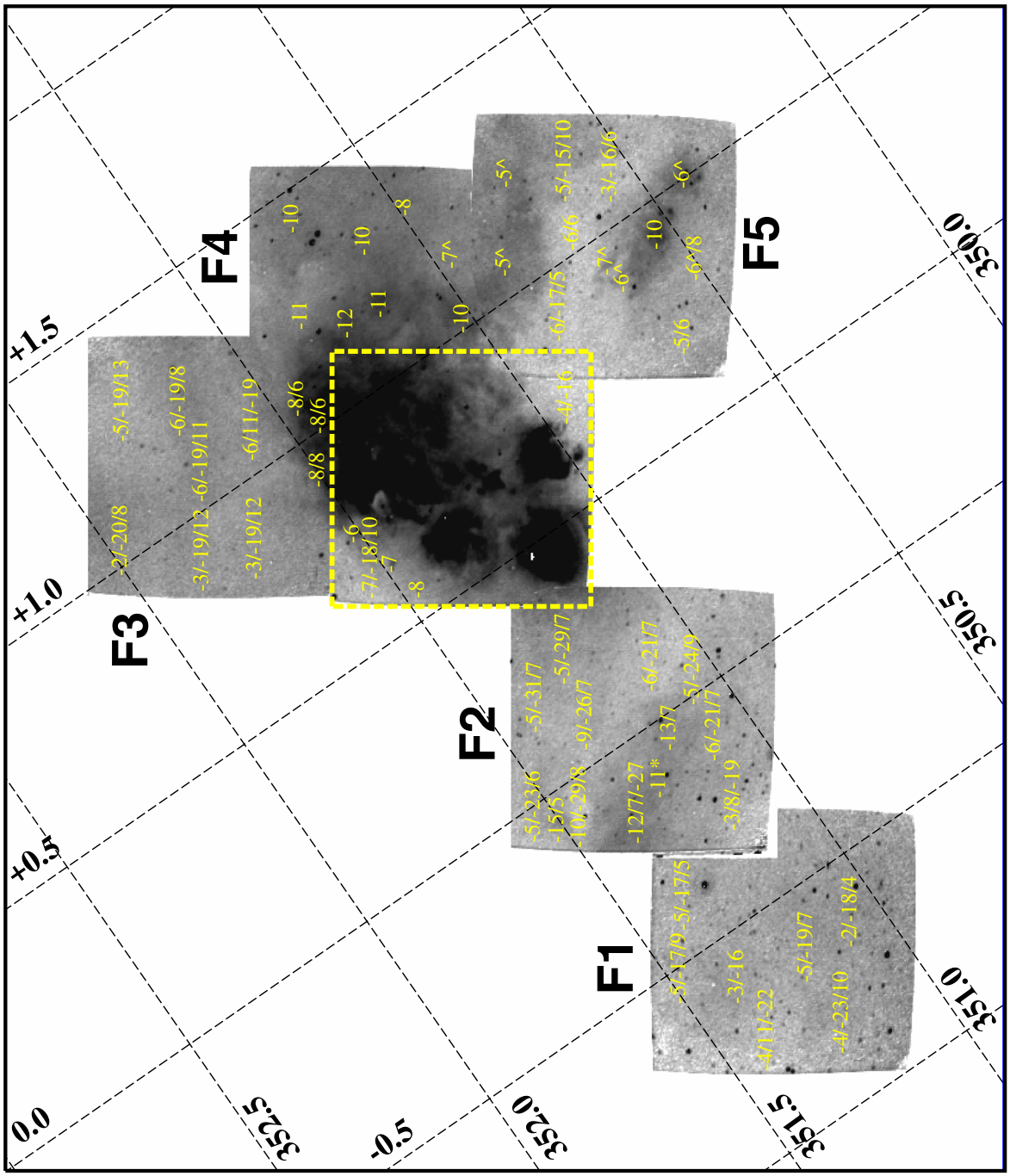

Fig. 2. Hα image of NGC 6334 (Galactic coordinates are indicated on the figure). The image was obtained by adding λ maps over the full spectral range, flat-fielding, and then correcting for distortion. This is equivalent to a photograph obtained through a filter with a 10 Å bandwidth. The central and most intense field is surrounded by a white square, while the other fields are labelled from F1 to F5. The numbers indicated on the image give the velocities of the three components that were fitted to the profile (ranked by decreasing intensity order) at this (central) position. When the number is followed by an asterisk or a hat symbol, this means that the fitted Gaussian has a FWHM that is significantly larger or thinner than 25 km s^{-1}, respectively.

The Molonglo Galactic Plane Survey[3] (MGPS) is a radio continuum survey (Green et al. 1999) made using the Molonglo Observatory Synthesis Telescope (MOST) at 843 MHz. The resolution is 43″ × 43″ cosec $|\delta|$. The typical sensitivity is 1−2 mJy/beam (1σ). The positional accuracy is 1−2″. Almost all of the unresolved or barely resolved objects are extra-galactic sources while the extended, diffuse emission is associated with thermal complexes, discrete H II regions, supernova remnants, and other structures in the Galactic interstellar medium.

3.2.2. ThrUMMS and HOPS data

ThrUMMS is a map of most of the fourth quadrant of the Galaxy with Mopra in four molecular species (^{12}CO, ^{13}CO, C^{18}O, and CN), at 72″ angular resolution, 0.1 km s^{-1} velocity resolution

[3] http://www.astrop.physics.usyd.edu.au/MGPS/

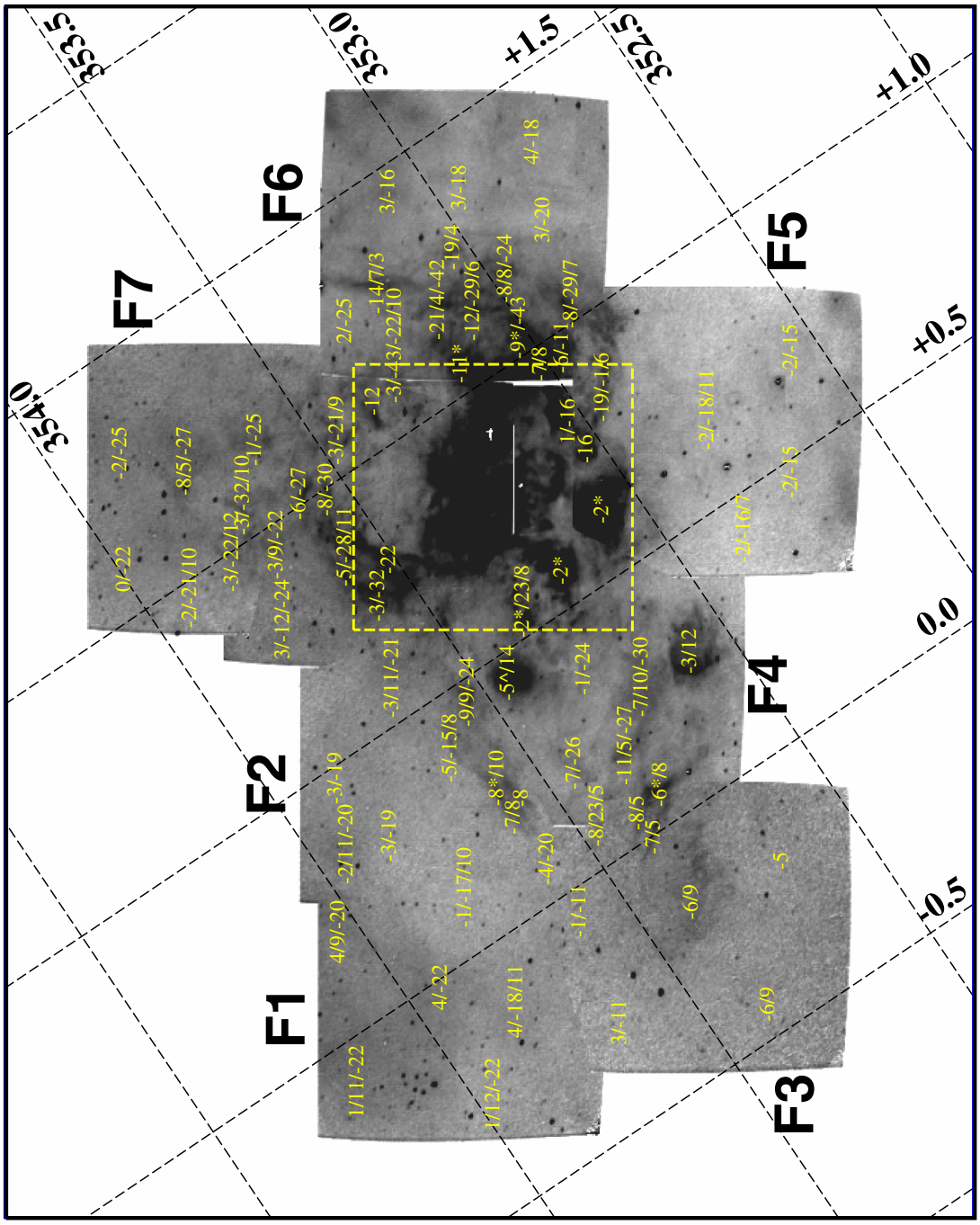

Fig. 3. Same as for Fig. 2 for the region NGC 6357.

and ~1.5 K km s^{-1} sensitivity. The data-cubes that are available at longitudes $l = 350°$ and $l = 352°$ do not cover NGC 6334 and NGC 6357 because the galactic latitude ranges of the survey is from $-0.5°$ to $+0.5°$ only. However we retrieved the ^{12}CO data-cubes [4] to determine the large-/medium-scale Galactic plane velocity components that are present along the line of sight.

The HOPS survey (Walsh et al. 2011) is a multi-line survey of the southern Galactic plane with Mopra observing simultaneously (with $\Delta v = 0.34$ km s^{-1}) in 16 molecular species at the frequency 27.5 GHz, including the H69α line. Owing to the limited latitude coverage, NGC 6334 and NGC 6357 are not covered except for part of the H II regions G353.08+0.28 and G351.2+0.5.

[4] http://www.astro.ufl.edu/~peterb/research/thrumms/rbank/

4. Preliminary data analysis

4.1. HI absorbtion spectra

To identify and determine the velocity components involved in the Hα profiles, we first identify the different gas layers that are present along the line of sight for both regions. Following the method of Strasser et al. (2007), we determine, from the SGPS, the absorbtion spectrum in the direction of the brightest parts of the continuum emission of NGC 6334 and NGC 6357. We

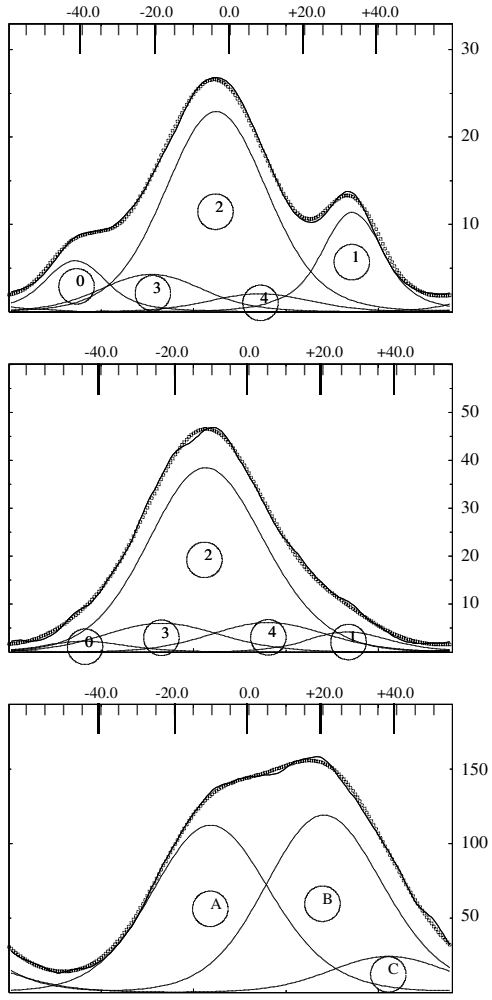

Fig. 4. Examples of Hα profile decomposition. The x-axis is the $V_{\rm lsr}$ (in km s^{-1}) and the y-axis is the intensity (in arbitrary units). The geocoronal Hα and OH night-sky lines are the components noted 1 and 0, while the nebular lines are noted from 2 to 4 (their sum is the square-dotted line). The lower panel shows, as an example, the profile from GUM 61 central area (see text).

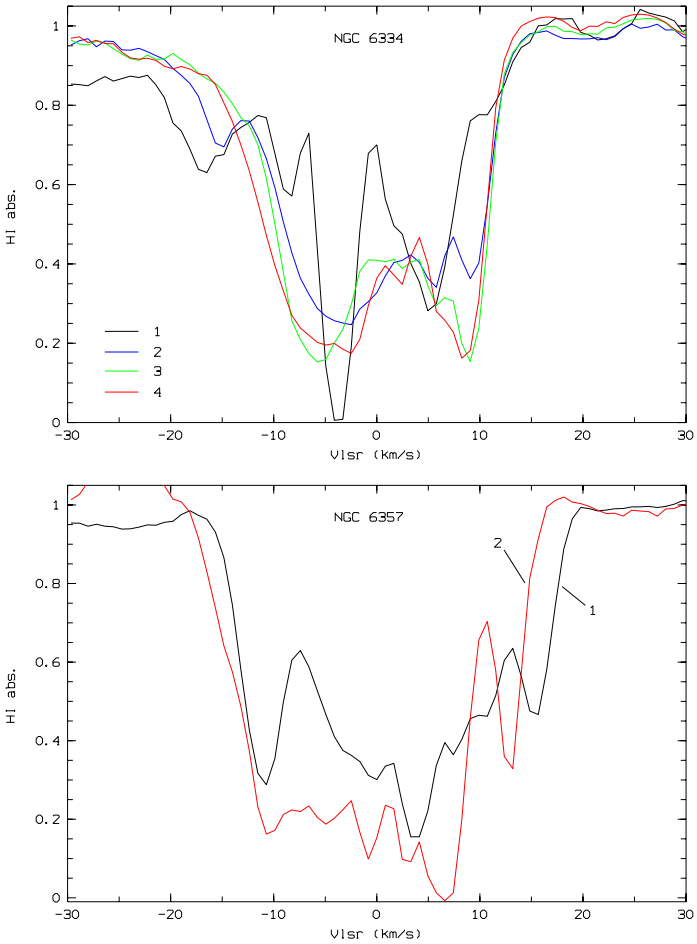

Fig. 5. HI absorption spectra. The individual extracted spectra are identified (by a number) as in Fig. A.1

extracted the average spectrum ("on" spectrum) from these positions and the average spectrum for background areas ("off" spectrum). The background areas are at about 20′and 30′ from NGC 6334 and NGC 6357, respectively (see Fig. A.1). The optical depth ($e^{-\tau}$) spectrum is then obtained by subtracting the "off" spectrum from the "on" spectrum and dividing this by the off-line continuum emission. The results are presented in Fig. 5. We are able to extract two and four spectra (with good signal/noise), respectively, in the direction of NGC 6357 and NGC 6334. The absorption spectra allow us to identify and study the foreground layers of HI gas. From these kinds of spectra we can determine the HI column density (Strasser et al. 2007):

$$N_{\rm HI} = 1.83\ 10^{18} \times T_{\rm s} \times \Delta V \times \sum \tau_V \qquad (1)$$

where $T_{\rm s}$ is the spin temperature (we assume a typical value, $T_{\rm s}$ = 125 K, following Foster and MacWilliams 2006) and ΔV is the velocity channel width (0.82 km s^{-1}). The visual extinction is derived by assuming the dust to gas ratio: $N_{\rm HI}/A_V = 1.5 \times 10^{21}$ cm^{-2} mag^{-1} (Bohlin et al. 1978).

For NGC 6357 the absorption spectra are very complicated and very broad below +10 km s^{-1} while distinct features around −10 km s^{-1}, +14 km s^{-1} (+12 km s^{-1} and +16 km s^{-1} in spectrum 1 and 2, respectively), and +5 km s^{-1} (+4 km s^{-1} and +6 km s^{-1} in spectrum 1 and 2, respectively) can be noted. We find a total $N_{\rm HI} \sim 9.9 \times 10^{21}$ cm^{-2} ($A_V \sim 6.6$ mag) for NGC 6357. Radhakrishnan et al. (1972) also noted the presence of a +6 km s^{-1} feature, which they attributed to a cold cloud in the foreground. They emphasised that this cloud covers an area of many square degrees since this +6 km s^{-1} feature is also observed in the direction of several dozens of sources that are situated, in projection, close to the galactic centre.

For NGC 6334 the absorption spectra show a clear feature around -4 km s^{-1}, which is in agreement with its systemic velocity. The column density of this layer is $N_{\rm HI} \sim 4.1 \times 10^{21}$ cm^{-2} ($A_V \sim 2.7$ mag). Features are noted also around +6 and +9 km s^{-1} that can be attributed to the foreground cloud noted by Radhakrishnan et al. (1972). These foreground layers exhibit $N_{\rm HI} \sim 2.3 \times 10^{21}$ cm^{-2} ($A_V \sim 1.5$ mag). Two other foreground components can be noted around −8.5 and −15 to −18 km s^{-1}, accounting for $A_V \sim 0.4$ each. However, we note that some features are only seen toward some of the pointings, which suggests that the extinction is patchy in the foreground of NGC 6334. The total extinction deduced for NGC 6334 is $A_V \sim 5.1$.

These A_V values are in agreement with the ones established from OB stars photometry (Russeil et al. 2010): 4.3 mag and 5.9 mag, respectively, for NGC 6334 and NGC 6357.

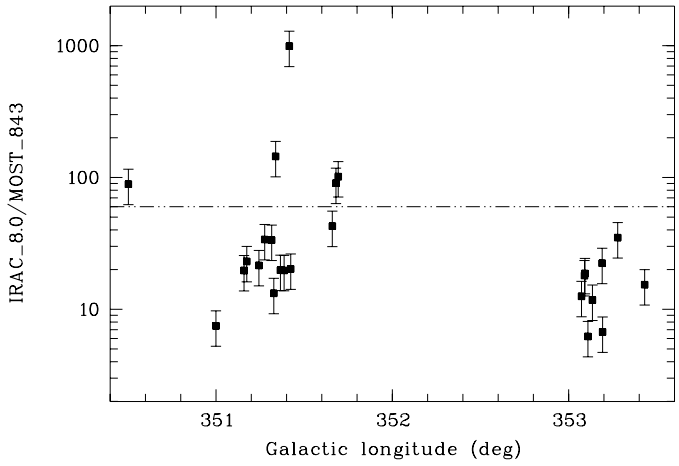

Fig. 6. *Spizer*-GLIMPSE 8.8 μm to the MOST 843 MHz flux ratio versus the galactic longitude. The dotted-dashed line shows the maximal flux ratio value (i.e. 60) expected for H II regions. The sources that belong to NGC 6357 have $l > 353°$, while the others ($l < 352°$) belong to NGC 6334.

4.2. Nature of the radio regions

We want to determine the nature of the ionized gas regions that belong to NGC 6334 and NGC 6357 star-forming complexes. First, we follow Cohen et al. (2007) to characterise the nature of the radio sources. Because supernova remnants show deficit of PAHs, they have low 8 μm emission when compared to H II regions. Cohen et al. (2007) determine an empirical 8.0 μm/843 MHz ratio of 0.14 for SNRs while this ratio is in general higher than 12 for H II regions (median values are between 20 and 60 depending on the H II regions type). Figure 6 shows this ratio for the radio sources in NGC 6334 and NGC 6357. They all have ratios larger than six. A ratio lower than 12 is found here for only three regions: GUM 61 (which is a very particular region as discussed in the next sections) and two compact sources in NGC 6357, which are located in the direction of pillars (as seen on 8.0 μm image). While sources in NGC 6357 do not exhibit a particularly large ratio, few sources with a ratio higher than 60 are found in NGC6334 and GM1-24, the region G351.41+0.64 (well known as the ultracompact H II region NGC 6334-I), which exhibits the largest value (Fig. 6). Cohen et al. (2007) interpret these extreme values as the result of optical thickness in the radio wavelength or being due to the fact that the region's exciting star(s) is strongly embedded in dust. The second explanation is favoured as Tapia et al. (1996) who observed a very young embedded massive star cluster in NGC 6334-I.

In other words, to determine if ionized gas emission is thermal (H II region) or synchrotron (e.g. supernovae remanent), we evaluate the spectral index following Reich and Reich (1988). We construct spectral index maps (Fig. 7) using radio continuum emission at two wavelengths: the 843 MHz MOST image and 1.38 GHz SGPS. After alignment, the 843 MHz map is convolved and resampled to the same resolution and pixel size as the 1.38 GHz map. Both maps are converted from Jy/beam to temperature scale. Because the absolute zero level of each involved image is not known, we determine the relative offset following Reich and Reich (1988) to compute a reliable spectral index map. We chose to scale the 843 MHz map to the 1.38 GHz one.

The spectral index is then calculated from:

$$\alpha = 2 - \log(T(\nu_1)/T(\nu_2))/\log(\nu_2/\nu_1), \quad (2)$$

where $\nu_1 = 1.38$ GHz, $\nu_2 = 843$ MHz, and α is the spectral index of the flux density ($S_\nu \propto \nu^\alpha$).

For non-thermal emission, α is expected to be negative ($\alpha < -0.1$) while for thermal emission, α is expected to be -0.1 (if optically thin) or larger (if optically thick). We evaluate a typical spectral index error $\Delta\alpha \sim 0.2$ from the intrinsic uncertainties of the radio map and the uncertainty on the offset. In addition, we have to bear in mind that some of the larger scale flux has implicitly been filtered out.

In addition to SNR, non-thermal extended radio emission was observed towards star-forming complexes and, at smaller scale, towards Wolf-Rayet nebulae. For example, non-thermal emission was observed in W43 and attributed to the winds from luminous stellar objects which, accelerating relativistic electrons, produce synchrotron emission (Luque-Escamilla et al. 2011). A negative spectral index was also observed towards the Wolf-Rayet nebula WR 21a and interpreted as being due to a colliding-wind process (Benaglia et al. 2005). Finally, unresolved collimated thermal ionized jets are expected to exhibit a spectral index between 2 and -0.1 (Reynolds, 1986).

For both regions we note that the spectral index changes from place to place, which is indicative of varying physical conditions. In NGC 6357 (Fig. 7, lower panel), non-thermal emission is found in the filamentary structures that faceing the cluster Pismis 24 and the region H II 353.09+0.63 which has been excited by the cluster AH03J1725-34.4.

In the NGC 6334 (Fig. 7, upper panel), the extended feature seen around $l = 351.69°$, $b = +0.92°$ corresponds to the well-known supernova remnant SNR351.7+0.8 (Green et al. 2006), which is located well behind NGC 6334 (Tian et al. 2007). Considering the optical H II regions, which are expected to be evolved H II regions, we note that all, except GUM61, have a positive mean spectral index, which suggests more or less optically thick thermal continuum emission. GM1-24 exhibits patches of emission with a negative index at the location of the radio source G350.50+0.9. A particular region is GUM 61. Its spectral index suggests a non-thermal emission as already noted by Carral et al. (2002).

Embedded in the NGC 6334 dust ridge, five compact radio sources also exhibit a negative spectral index (this kind of negative spectral index has been also observed recently by Rodriguez et al. 2014 for the radio source NGC 6334A) but their 8.0 μm/843 MHz ratio suggests that a supernova remnant nature is unlikely. Because the ridge is clearly a star-forming region (e.g. Carral et al. 2002; Russeil et al. 2010), their non-thermal emission could be attributed to shocks that were induced by outflows and/or winds.

5. Hα Kinematics of the regions

5.1. General aspects

For NGC 6357 the kinematics of the molecular gas spans between -10 and $+2.5$ km s^{-1} (Cappa et al. 2011) with a main velocity at -4 km s^{-1} (Massi et al. 1997) while, for NGC 6334, this is between -13 and $+3$ km s^{-1} with a main velocity at -4 km s^{-1} (Kraemer & Jackson, 1999). In the direction of NGC 6334, CO surveys (Dame et al. 1987, Robinson et al. 1988; Kraemer & Jackson 1999) show, in addition to the velocity of NGC 6334 and NGC 6357, components at $V_{\rm lsr} \sim -25$, -40 and -125 km s^{-1}, respectively. Because these components are not seen in HI absorption spectra (see Sect. 4.1) they can be attributed to background layers. From CO longitude-velocity plots (Bitran et al. 1997), a molecular component is also noted

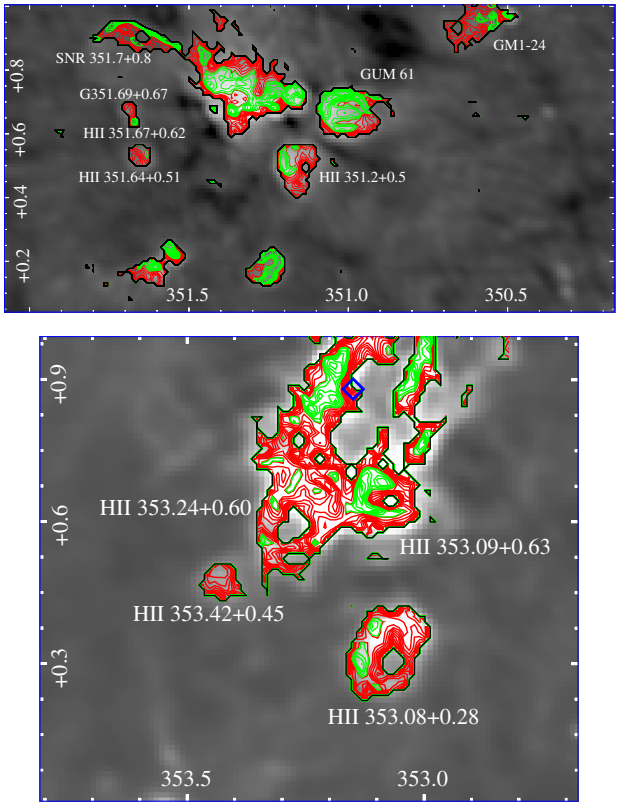

Fig. 7. Spectral index maps (in galactic coordinates) of NGC 6334 (*upper panel*) and NGC 6357 (*lower panel*). The green and red isocontours trace $\alpha \leq -0.2$ and $\alpha > -0.2$, respectively. The main H II regions and, for NGC 6357, the cluster Pismis 24 (blue diamond in the *upper panel*) are indicated.

around +9 km s^{-1} (extended from $b = +0.25°$ to $b = +2.25°$ and $l = 350°$ to $l = 354°$) while the molecular complex, to which NGC 6334 and NGC 6357 belong, is well identified at ∼−5 km s^{-1}.

The analysis of ThrUMMS ^{12}CO data (Fig. A.2) allows us to specify the molecular distribution between $b = -0.5°$ to $b = +0.5°$. We note a narrow-line component around +6 km s^{-1}, a broad-line component around −20 km s^{-1} (more intense at low/negative latitudes) and several broad features with velocity that is more negative than −40 km s^{-1}. In addition, a component at −5 km s^{-1}, for $l = 350°$−$351.9°$) can be clearly associated with NGC 6334. For $l = 352°$−$354°$, two peaks around +1 km s^{-1} ($b = -0.5°$−$+0.5°$) and −3 km s^{-1} ($b > 0.2°$), respectively, are noted. The last one can be associated with NGC 6357, while the former one is a different emission along the line of sight as a result of its latitude extension.

Optical dark clouds (Otrupcek et al. 2000), in the longitude range between NGC 6334 and NGC 6357, are found with velocity ∼+6.2 km s^{-1} with quite constant intensity ($T_A^* \sim 9.4$ K) and narrow width (*FWHM* ∼ 1.3 km s^{-1}). Such quiescent clouds, observed up to $b = 4.4°$, belong to a foreground molecular layer. Dark clouds with velocities around −20 km s^{-1} (FWHM between 3.1 km s^{-1} and 8.6 km s^{-1}) and with velocities between −4.2 and 0.4 km s^{-1} (*FWHM* ∼ 2 km s^{-1} to 8.6 km s^{-1}) are also found in directions pointing close to NGC 6334 and NGC 6357.

Foreground clouds are also detected in several molecular species towards NGC 6334I (e.g. Zernickel et al. 2012) as H_2O (−6.3 km s^{-1}, −0.3 km s^{-1}, and +6.2 km s^{-1}, Emprechtinger et al. 2010) or CH (−3 km s^{-1}, 0 km s^{-1}, +6.5 km s^{-1}, and +8 km s^{-1}, Van der Wiel et al. 2010) absorption components. Emprechtinger et al. (2013) interpret the +0 km s^{-1} as a component that most likely originates in the local environment of NGC 6334-I, associating the other features with foreground clouds. The OH absorption feature at +6 km s^{-1} is also reported towards several NGC 6334 cores (Brooks & Whiteoak 2001) and on the line of sight of the pulsar PSR B1718-35, which is located to the east of NGC 6334 (Minter 2008). The HI data (Sect. 4.1) also confirm that the gas layer around +6 km s^{-1} is foreground.

The above results can be summarised as follows:

1. The ∼+6 km s^{-1} velocity component is a foreground extended layer of gas that is not related to NGC 6334 and NGC 6357.
2. The origin of the diffuse component around −20 km s^{-1} is not clear, but it probably originates from the galactic plane.
3. Velocity components around and more negative than −40 km s^{-1}are due to background emissions.
4. Velocities between −11 km s^{-1} and 0 km s^{-1} trace the NGC 6334 and NGC 6357 complex. When seen in absorbtion, they trace clouds that reside in the local environment of the regions.

In the following, we aim to determine the kinematics using the Hα data cubes, but we have to bear in mind that the galactic longitude of NGC 6334 and NGC 6357 makes the analysis difficult. This is because, as a result of the galactic longitude of the regions (near the galactic center direction), the typical internal velocities (∼±6 km s^{-1} around the systemic velocity) and systemic velocities (∼−4 to −9 km s^{-1}) have similar values. In addition, in Hα, the local component, located around 200 pc (see, e.g. Russeil et al. 2005), is expected to have a velocity of −5 km s^{-1}, which is also similar to the mean velocity of NGC 6334 and NGC 6357, which are located farther away.

To understand the kinematics of the H II regions we use, three approaches to analyse the Hα data in the following sections:

1. To increase the S/N, the first approach consists of extracting and decomposing the Hα profiles in area delimitating conspicuous structures (see Sect. 5.2). The velocity of the three components is indicated in Figs. 2 and 3, while their FWHM is forced on 25 km s^{-1} except in a few positions where a larger/narrower Gaussian is required.
2. Towards the central zone of NGC 6334 and NGC 6357, the intensity is high and the velocity field is very complicated. For these zones, we adopt a second approach (see Sect. 5.3) to determine the velocity field, which is to extract and decompose the profiles through a regular grid (45″ × 45″ cells). The decomposition was led with an automatic process that consists of the χ^2 minimizing, using the routine "Minuit" (Nelder & Mead 1965). We impose and fit the profiles with 3 nebular (Gaussian) components. We then produce a velocity field and FWHM maps from this automatic profile decomposition (Figs. 8 and 9).
3. The third approach consists of studying the velocity dispersion (σ) versus intensity plots (see Sect. 5.4). In addition to the central field, the automatic fitting is applied to fields F5 and F4 of NGC 6334 and NGC 6357 (Figs. 2 and 3). To arrive at an adequate S/N in these fields, we extracted the profiles throught a regular grid of 11 × 11 pixels (99″ × 99″ cells).

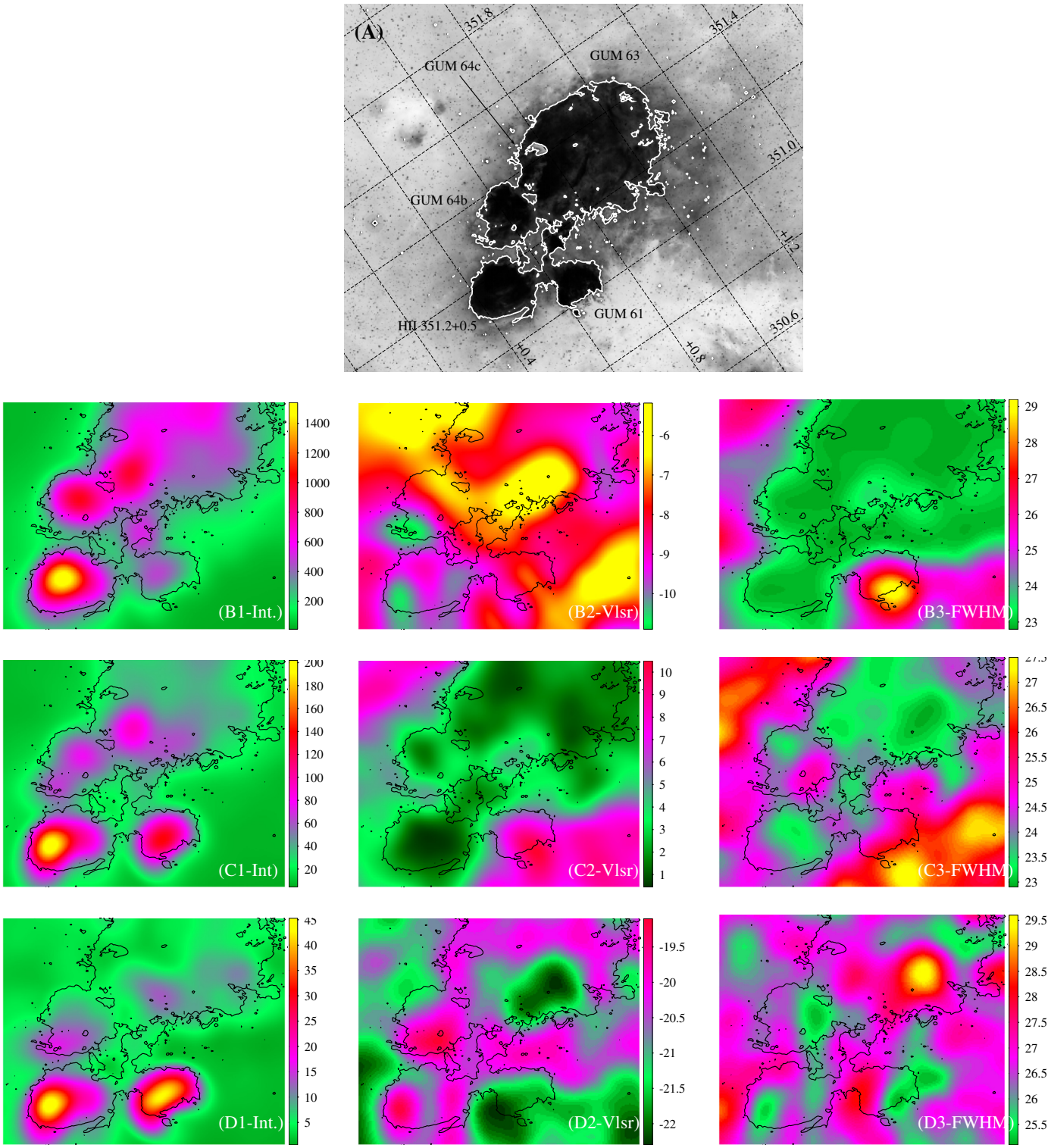

Fig. 8. Panel **A)**: NGC 6334 with the name of the different regions and an intensity isocontour Panel **A)** is used as reference to the other panels. The galactic coordinates are also indicated. NGC 6334 intensity (panels **B1)**, **C1)**, and **D1)**), velocities (panels **B2)**, **C2)**, and **D2)**) and FWHM (panels **B3)**, **C3)**, and **D3)**) maps of the three components. Intensity is in arbitrary units while velocities and FWHMs are in km s^{-1}.

5.2. General Hα analysis

5.2.1. NGC 6334

The first step to analyse the kinematics of the region is to determine the number and the kinematics of the diffuse emissions that are present along the line of sight. Figure 2 shows the Hα emission with a high contrast to highlight the faint diffuse emissions. The Hα profiles from the diffuse emission that surrounds the main region (Fig. 2, fields F1 to F5) are decomposed into three components (of mean velocity −6 km s^{-1}, −20 km s^{-1}, and +8 km s^{-1}) which are indicated (sorted by decreasing intensity) at the position of the features. Generally, we note that the positive velocity component, which is the faintest one most of the time, is also not systematically

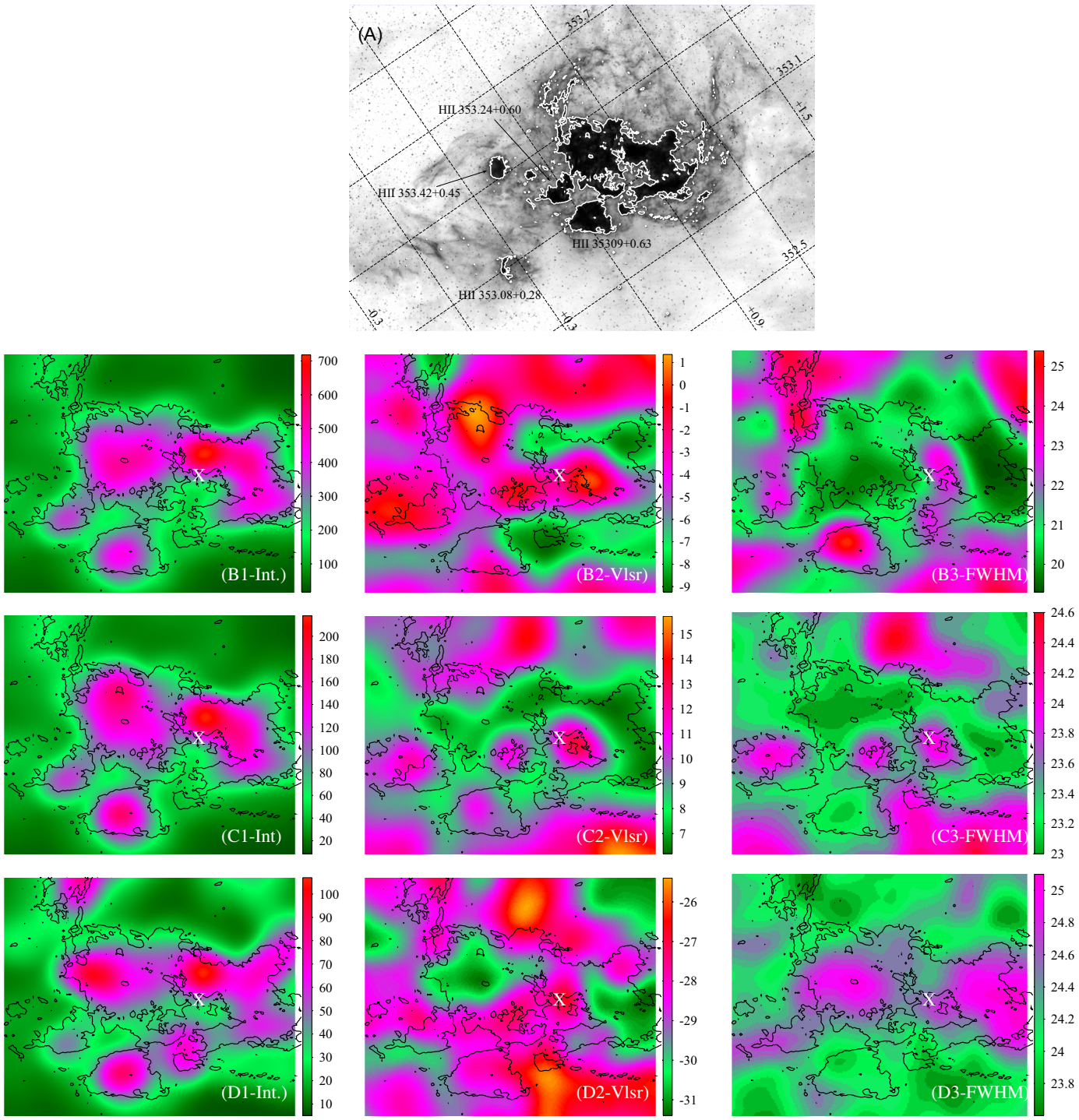

Fig. 9. Same as for Fig. 8, but for NGC 6357. The position of Pismis 24 is indicated by the white cross.

required to perform the fit, suggesting it is inhomogeneously distributed.

Field F1: This field, which shows no structured features, is ideal for identifying the different diffuse emission layers present along the line of sight. The decomposition of profiles (illustrated in Fig. 4, upper panel) gives the three components at the mean velocities of -5 km s^{-1}, -19 km s^{-1} and $+8$ km s^{-1}, and with a quite constant intensity throughout the field. The most intense is the -5 km s^{-1} component with a typical intensity of 3.5 and 7 times larger than the -19 km s^{-1} and $+8$ km s^{-1} components.

Field F2: In this field the three components have mean velocities of -7.5 km s^{-1}, -25 km s^{-1}, and $+7$ km s^{-1}. In particular the elongated Hα feature around l, b = 351.302°, −0.137° (17h23m45.6s, −36°19′19.2″) has a velocity of -12 km s^{-1}. We also note two extinction patches around l, b = 351.449°, −0.077° (17h23m54.5s, −36°09′52″) and l, b = 351.075°, −0.110° (17h22m06.2s, −36°22′06″) towards which all the components are strongly attenuated, suggesting that these extinction features are in front of, and not related to, NGC 6334.

Field F3: This field is to the north of the most intense part of NGC 6334. The three components are found at mean velocities of −4 km s^{-1}, −19 km s^{-1}, and +11.5 km s^{-1}. The last two have quite constant intensity through the field, while the −4 km s^{-1} component is more variable as can be seen by the smooth emission features on the image.

Fields F4 and F5: The field F4 covers the western border of the extented H II region GUM 63. The Hα intensity is high and dominated by the emission of the H II region with a mean velocity of −10 km s^{-1}. The field F5 covers the H II region GM1-24, for which we can determine a systemic Hα velocity of −9 km s^{-1}, as well as a strong extinction area. Several positions exhibit smaller (*FHWM* = 20 km s^{-1}) Hα line width. They correspond to GM1-24 edges and several positions along the northern edges of the strong extinction area. This type of narrow line can underline a strong interaction between the ionized and molecular gas at these positions. Indeed, Westmoquette et al. (2013) show that narrow Hα lines are found toward pillars and seem to originate from gas near to (deeper, denser) neutral/molecular layers that is just being ionized. This interpretation is in agreement with the location of the compact source G350.615+0.832 at the GM1-24 edge in this type of narrow Hα line area.

According to Sect. 5.1, the +8 km s^{-1}and the −25 km s^{-1} Hα emission can be attributed to foreground and background layers, respectively, while the −6 km s^{-1} is the diffuse emission belonging to the same layer as NGC 6334.

5.2.2. NGC 6357

We follow the same approach as for NGC 6334 to analyse the diffuse emission Hα profiles. Figure 3 shows the Hα emission with a high contrast to highlight the faint diffuse emissions and the components' velocities are indicated (sorted by decreasing intensity) at the position of the features. Generally, we note that the kinematics of NGC 6357 are clearly more complicated than for NGC 6334, as also suggested by its strong filamentary morphology (as seen in Hα). In addition, Cappa et al. (2011) identified several molecular clouds in the direction of NGC 6357 with velocities of between −12.5 and +2.5 km s^{-1}. In particular we notice their shell A and cloud C with a velocity of between −7.5 and +2.5 km s^{-1}.

Field F1: We start the analysis with this field because it is the farthest from NGC 6357 itself and it only shows diffuse features. Three components with mean velocities +3 km s^{-1}, −21 km s^{-1}, and +11 km s^{-1} are observed. With the most intense features in this field being at +3 km s^{-1}, it is difficult to know if they are related to the +6 km s^{-1} foreground layer, to an other gas layer, or to NGC 6357. We favour the second explanation since the morphology of these emissions is very different to the ones observed towards NGC 6357. The +11 km s^{-1} is encountered in other fields in better agreement with the larger scale +6 km s^{-1} foreground layer, and Cappa et al. (2011) detected ^{12}CO emission with a velocity of between 0 and +2.5 km s^{-1}.

Fields F2, F3, and F4: These fields allow us to probe the Hα kinematics of diffuse layers, filamentary and patchy structures, as well as the H II regions, H II 353.08+0.28 and H II 353.42+0.45. The filamentary structures and patches all have the same mean velocity of –8 km s^{-1} with an additional positive velocity component always observable. This can be interpreted as tracing the wing of the line instead of an unrelated layer present on the line-of-sight. In Hα the region H II 353.42+0.45 has a quite spherical morphology with its intensity centrally peaked. The exciting star of this region is identified by Gvaramadze et al. (2011) as a running away star. Its systemic velocity is −5 km s^{-1}. The +14 km s^{-1} component (Fig. 3) represents only 5% intensity of the −5 km s^{-1} one. In Hα, the region H II 353.08+0.28 appears as a bright Hα rim, on its west side, and a fainter more diffuse emission on the east side (Fig. 13). A large portion of the region, as seen in radio (Fig. A.3), is not optically visible because of extinction. Thanks to the H69α, line we can follow its kinematics in the faded parts and note that the Hα and H69α velocities are in agreement and give a systemic velocity of −3 km s^{-1}.

Field F5: Three diffuse components around −2 km s^{-1}, −16 km s^{-1}, and +8.5 km s^{-1} are observed in this field. They are mainly diffuse components. The +8.5 km s^{-1} is present only in the northern part of the field.

Field F6: In this field, corresponding to the eastern edge of NGC 6357, filamentary and patchy structures are noted with a strong velocity mixing: some filaments and patches are at ∼8 km s^{-1}, while others are around −22 and −14 km s^{-1}. This suggests that this area is kinematically complex and could be the most impacted by the large energy that is issued from the central parts.

Field F7: This field, corresponding to the northern edge of NGC 6357, is dominated by Hα patches with velocities of between −3 and −8 km s^{-1}. An additional component at −25 km s^{-1}is seen everywhere with large intensity increases (×5) in the patches underlining a systematic blue wing for the Hα line. The large arc-like structure, around l, b = 353.538°, +0.767° (17h26m14.37 s, −33°57′48.7″) shows a large velocity gradient, as underlined by the −3 km s^{-1}and −22 km s^{-1}velocities on its northern and southern sides, respectively.

In Fields F6 and F7, some profiles have very large FWHM (30 to 35 km s^{-1}) and in a few places, up to four components are required to perform the fit with, for some of them, extreme (∼−43 km s^{-1}) velocities. The velocity-mixing of the filaments and patches in fields F6 and F7 suggests a 3D geometry and strong Hα profiles asymmetry.

5.3. Central zone kinematics

For this analysis, we follow Rozas et al. (2006) who observe that the Hα profile from extra-galactic H II regions usually needs to be decomposed with three Gaussian components: a bright, central component and two roughly symmetric fainter components (also considered as line wings), displaced to higher (absolute) velocities. They interpret the main emission component as coming from the bulk of the H II region while the wings are attributed to an expanding shell. The expansion velocity of the regions is then defined as the mean velocity of the wings with respect to the central kinematic component. Here, because we observed the larger scale diffuse Hα emission, we suppose that the most intense component traces the main gas motion, while the other two are either diffuse layers, when observed apart from H II region, or tracing the line wings, when observed in the direction of the individual H II regions.

5.3.1. NGC 6334

The automatic fitting process, applied to the central zone, allows us to analyse the kinematics (Fig. 8) of the regions GUM63, GUM64b, GUM61, and H II 351.2+0.5.

GUM64b: In Fig. 8B2 a clear velocity gradient from -5 km s^{-1} to -11 km s^{-1} (orientated North-West to South-East), is clearly visible for GUM64b. This behaviour is typical of gas flow for a region in its "champagne" phase (Tenorio-Tagle 1979; Bodenheimer et al. 1979). The morphology of the flow suggests that its ionizing star(s) is/are located near or in the molecular cloud ridge.

GUM61: Figure 8B3 shows a quite constant FWHM throughout all the fields except towards GUM61 where the FWHM is larger, changing from $FWHM = 29.5$ km s^{-1} at $l, b = 351.007°, +0.651°$ (defining the kinematic centre position) to $FWHM = 25$ km s^{-1} on the edges. In Fig. 8B2, a systemic velocity of -9 km s^{-1} can be deduced. In Fig. 8C2, the second component shows a velocity gradient from 6 to 10 km s^{-1}, which is associated (panel C3) with a small but noticeable FWHM increase (from the north-east to the south-west). This suggests that in addition to the global expansion there is a flow motion in the opened direction of the nebula. The component at -22 km s^{-1} (Fig. 8D2) shows no significant velocity variation. Towards the optical centre, the automatic fitting process gives a different profile decomposition from the one given in Fig. 4, but the deduced expansion velocity is similar.

In summary, GUM 61 is a bubble in expansion but with a kinematic centre that is different from the optical emission centre (for which the exciting stars were supposed to be the HD319703 binary). This kinematic centre is in better agreement with the geometric centre of the region as seen in radio and *Herschel* 70 μm emission (Russeil et al. 2013), which are not sensitive to the extinction (Fig. A.4). In addition GUM61 is catalogued by Churchwell et al. (2007) as the "broken ring" CS94 (radius 5.26′ and shell thickness 0.91′), whose centre is in agreement with our kinematic centre.

H II 351.2+0.5: From Fig. 8B1, H II 351.2+0.5 is the brightest H II region. This exhibits (Fig. 8B2 and B3) a main component with a constant FWHM (23.5 km s^{-1}) and a velocity between -8.5 km s^{-1} and -13 km s^{-1} (east edge) in agreement with the radio line velocities (Fig. A.3). However, from Fig. 8B2 one can kinematically distinguish the central zone (~ -9 km s^{-1}) from the east (~ -13 km s^{-1}) and west (~ -10 km s^{-1}) sides. This small but noticeable velocity difference could be due to the fact that H II 351.2+0.5 can be divided into two H II regions, seen from *WISE* 22 μm (Fig. A.4) emission corresponding to each of these two sides. Hot stars are identified towards these two H II regions: HD156738 (O6III((f)), Sota et al. 2014) and ALS 4095 (B1e, from Neckel 1978). The eastern region is the largest one. It corresponds to the brightest part of H II 351.2+0.5 in Fig. 8C1 and D1 and to a velocity decomposition of -13 km s^{-1} (in Fig. 8B2) and -19 km s^{-1} (in Fig. 8D2). This location is also detected in H69α (Fig. A.3) suggesting that it is a dense area. On the *Spitzer*-8 μm image, it corresponds to a zone located between a bright rim and the small ($R_{\rm eff} = 0.66'$) infrared bubble CS90 (Churchwell et al. 2007) within H II 351.2+0.5. The binary star HD156738 (Sana et al. 2014) is centred in CS 90 and could have formed this bubble. The second H II region is also identified as an infrared bubble (MWP1G351131+005267, $R_{\rm eff} = 1.47'$) by Simpson et al. (2012) centered on ALS 4095. However the size of these bubbles is small compared to the full ionized gas extension of H II 351.2+0.5 ($R_{\rm eff} \sim 5.6'$), which suggests they could be evolving inside a previously ionized region. We can estimate a rough and global expansion velocity of 10 km s^{-1} for H II 351.2+0.5 in agreement with Johnson (1982) who gives an upper limit expansion velocity of 6 km s^{-1}.

GUM63/GUM64c: Defined here as the 34 arcmin size extended emission north-west to the ridge, its kinematics is difficult to interpret. The Fig. 8B2 shows velocities between -5 km s^{-1} and -9 km s^{-1} and all the filaments have a velocity of around -8 km s^{-1}. The -5 km s^{-1} velocity is found around $l, b = 351.239°, +0.832°$ (17h19m38s, $-35°49'19''$) a location corresponding to an infrared dark cloud (Dutra and Bica 2002). The fact that no extinction is noted in Hα suggests that the ionized gas is either at the front of the dark cloud or that the dark cloud could be a cavity that is filled by ionized gas (we note no structured emission toward the dark cloud from WISE-22 μm to *Herschel*-500 μm emission). However, no organised motion, like expansion or flow, can be detected for the GUM63/GUM64c area.

5.3.2. NGC 6357

The automatic fitting procedure applied to the central zone in Fig. 9 embables us to analyse the kinematics of the ionized gas in directions around Pismis 24 and the regions H II 353.09+0.63 and H II 353.24+0.60.

The ionized gas around Pismis 24: In panel Fig. 9B2, the well-known stellar cluster, Pismis 24 is located within a -2 km s^{-1} ionized gas patch surrounded by a semi-ring like velocity feature at -8 km s^{-1} (panel B2). This feature corresponds spatially to the CO shell A and cloud C of Cappa et al. (2011) detected between -7.5 and $+2.5$ km s^{-1}. The velocity and spatial agreement between the ionized and CO gas underlines their interaction. In Fig. 9B3, the west side of NGC 6357 exhibits narrower FWHM, which spatially corresponds to the brightest part of shell A (Cappa et al. 2011). This suggests a strong interaction between the ionized and molecular gas at this position. The Hα brightest part of NGC 6357 is the region around $l, b = 353.184°, +0.896°$ (17h24m45.8s $-34°11'04.1''$) facing Pismis 24 where pillars are observed (e.g. Bohigas et al.2004). This position is clearly visible in the three components with velocities around -3 km s^{-1}, $+11$ km s^{-1}, and -28 km s^{-1} respectively. These velocities match the higher spatial resolution Hα observations of the pillar by Westmoquette et al. (2012) but they could more closely trace the velocity of the small blister region that is located about 20″ north of the pillar. In this way, the region would present internal motion of about 19 km s^{-1}.

H II 353.09+0.63: This region exhibits (Fig. 9B2) a central velocity of -3 km s^{-1} while its west and east edges are at -7 km s^{-1}, which could indicate the interaction of this H II region with two adjacent molecular clouds, as seen in Fig. 8 of Cappa et al. (2011). Bearing in mind that the second ($+10$ km s^{-1}) and third (-27.5 km s^{-1}) Hα components have significant intensities only in the central part (panels C1 and D1), we estimate an expansion velocity of about 18 km s^{-1}.

H II 353.24+0.60: This region exhibits (Fig. 9B2) a systemic velocity of ~ -2 km s^{-1}. Figures 9B2 and C2 suggest a kinematical centre ($l, b \sim 353.26°, 0.57°$) offset respectively to the brightest Hα emission, which is in better agreement with the CS61 IR-bubble centre (Churchwell et al. 2007). This could be due to extinction, since from the radio continuum map this region shows a different morphology (ring-like) from its very patchy Hα aspect. Given the fact that the second ($+10$ km s^{-1}) Hα component has significant intensity only

(panel C1), we determine a minimal expansion/gas flow velocity of about 10 km s^{-1}.

5.4. Optical H II regions velocity dispersion

Non-thermal motions in H II regions are due either to turbulence or large-scale velocity gradients. Such velocity gradients in H II regions are usually associated with the "champagne" effect or the expanding shell that is attributed to strong stellar winds. Another approach for studying the kinematics of ionised gas is to use the velocity dispersion (σ) versus intensity plot (Iσ plot) as a diagnostic of the evolution status and the nature of the regions (Muñoz-Tuñón et al. 1996).

In these Iσ plots, so far performed for extragalactic H II regions complexes, Muñoz-Tuñón et al. (1996) and Moiseev and Lozinskaya (2012) show that the low density turbulent ISM appears as a low intensity vertical band, while the shell-like structures (as SNR and WR) can be distinguished as narrow inclined vertical bands (the younger the shell, the longer the strip) and H II regions are expected to draw horizontal features (see Fig. 6 of Moiseev and Lozinskaya 2012).

Following Moiseev and Lozinskaya (2012), we trace each cell's profile in this kind of Iσ plot for the fields that cover the brightest parts of NGC 6334 and NGC 6357 (Figs. 10 to 13). For this we converted the FWHM into velocity dispersion ($\sigma_{\rm obs} = FWHM/2.3548$) and corrected it ($\sigma^2 = \sigma^2_{\rm obs} - \sigma^2_{\rm nat} - \sigma^2_{\rm ther}$) for the natural width ($\sigma_{\rm nat}$ = 3 km s^{-1}, O'Dell & Townsley 1988) and for the thermal width $\sigma_{\rm ther}$ linked to the temperature of the region (T = 6500 K and 6100 K for NGC 6334 and NGC 6357 respectively, taken from Schraml & Mezger 1969). For each field, we divide the plot into a high and low dispersion regime when σ is respectively larger and smaller than $\sigma_{\rm m}$ (where $\sigma_{\rm m}$ is the intensity-weighted dispersion), and into high and low intensity emission when the flux is respectively larger and lower than the mean flux value in the field (see the color coding in Figs. 10 to 13). Till now, the velocity dispersion of H II regions has been studied in extra-galactic H II regions or H II regions complexes (e.g. Lagrois et al. 2011; Rozas et al. 2006; Relaño et al. 2005) by probing their kinematics at a scale of several tens to several hundreds of parsecs. This is the first time that this approach has been applied to galactic H II regions. For extra-galactic H II regions, the mean σ is 10–50 km s^{-1} (Arsenault et al. 1988, Moiseev & Lozinskaya 2012; Rozas et al. 2006; Blasco-Herrara et al. 2010).

In Figures 10 to 13, we note that the majority of the positions have σ less than the typical sound speed expected for ionized gas (~10 km s^{-1}). We can estimate that 3% to 34% of the profiles exhibit σ > 10 km s^{-1}, while for the diffuse emission (Figs. A.8 to A.11) this is between 25% and 70% (with a mean value of 50%). The central part of NGC 6357 (Fig. 12) appears as the most turbulent area. In Figs. A.8 to A.11, which is traced for pure diffuse components (belonging to gas layers present along the line of sight), and the part of the fields covering the surroundings of the H II regions in Figs. 10 and 11, we confirm that the vertical distribution at low intensity is attributed to the diffuse emission and that σ reaches maximum values in such diffuse medium, which is similar to extra-galactic studies.

GUM61 and H II 353.09+0.63 (Figs. 10 and 12) exhibit vertical features that confirm that they are shell-like regions. Inversely (Figs. 10 and 13) the regions GUM64b, H II 351.2+0.5, H II 353.08+0.28 and H II 353.42+0.45 exhibit horizontal features, which suggests that they are typical H II regions. In addition, we note that the points corresponding to H II 351.2+0.5 (Fig. 10) are, in general, below the GUM64b

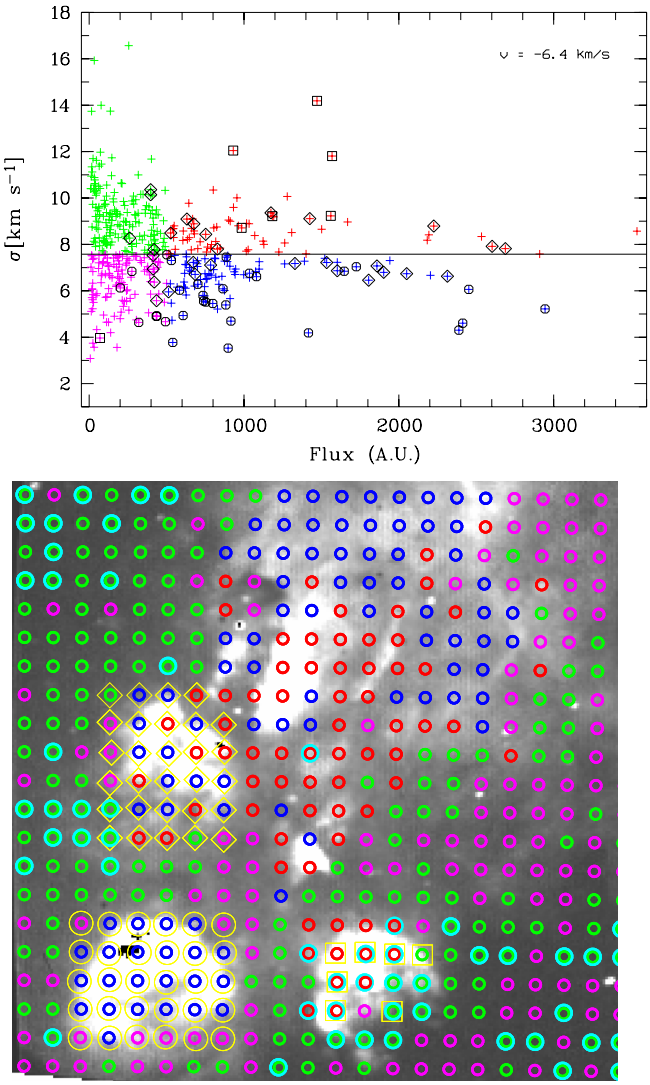

Fig. 10. *Top*: NGC 6334 central area σ versus flux diagram. Fluxes are in arbitrary units. The horizontal line is $\sigma_{\rm m}$ (see text). *Bottom*: the location of the zones identified by different colors on the σ – flux plot overlaid on the image. North is up and East is to the right. In this field 12% of the profiles show σ > 10 km s^{-1}. The positions where σ > 10 km s^{-1} are underlined in cyan. In both panels, the points overlaid with square, lozenge and circle symbols belong to GUM 61, GUM 64b, and H II 351.2+0.5 respectively.

ones, which is in agreement with an increase of σ with the H II region expansion.

Following Lagrois et al. (2011), for individual H II regions we compare (Fig. 14 and Table 1) the one-standard deviation of the centroid distribution $\sigma_{\rm vel}$ of the main Hα component (which quantifies the velocity variation on the plane of the sky) with the non-thermal velocity dispersion, σ, issued from the line width. Lagrois et al. (2011) plotted $\sigma_{\rm vel}$ versus σ for models (for different inclination angles) of H II regions with champagne flow only or with champagne flow perturbed by an expanding wind-blown bubble. We clearly see (Fig. 14) that GUM61 is strongly wind-dominated. However, by comparing Hα and radio emission, we note that H II 353.08+0.28, H II 353.24+0.60, and GUM61 are affected by extinction, which suggests we cannot follow the velocity variation on the full sky extension of the H II region. As a result, their $\sigma_{\rm vel}$ may have been underestimated.

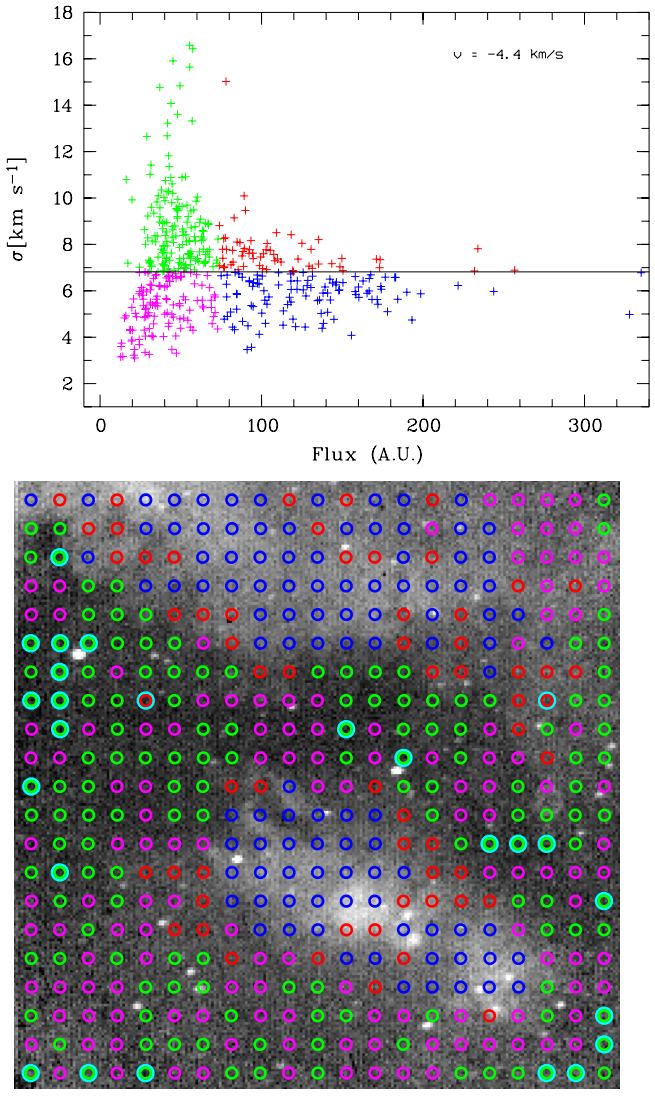

Fig. 11. Same as Fig. 10, but for GM1-24. In this field, 7% of the profiles show $\sigma > 10$ km s^{-1}.

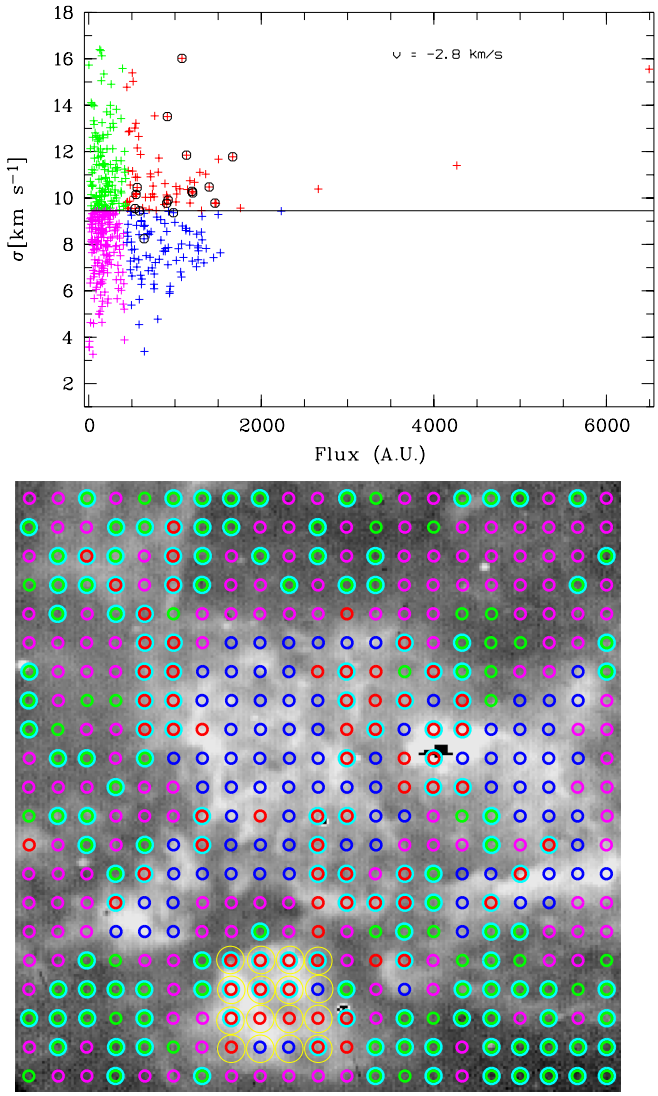

Fig. 12. Same as Fig. 10, but for the central part of NGC 6357. The points overlaid with circles belong to H II 353.09+0.63. In this field 34% of the profiles show $\sigma > 10$ km s^{-1}.

Assuming a 100% underestimation of $\sigma_{\rm vel}$, we can conclude that H II 353.08+0.28 could also be a wind-dominated H II region.

6. Discussion

From our previous analysis we suggest that optical H II regions impact the local ISM differently. In NGC 6334, we saw that GUM 61 is probably an expanding wind-driven shell H II region, GUM 64b is an H II region in "champagne" phase, and H II 351.2+0.5 is the grouping of two H II regions. In NGC 6357, the four well-defined H II regions can be listed: H II 353.42+0.45 is a centrally peaked H II region (associated with a run-away star), H II 353.08+0.28 and H II 353.09+0.63 (which are probably wind-dominated H II regions), and H II 353.24+0.60 (which exhibits a very patchy morphology in Hα). H II 353.09+0.63 is powered by the cluster AH03J1725-34.4, while H II 353.08+0.28 seems to be powered by a single source (Townsley et al. 2014). In Table 1, we summarise the properties of the radio sources (from MGPS and SGPS surveys) and the optical H II regions located in NGC 6334 and NGC 6357. Some radio sources correspond to optical H II regions but, because of extinction, the coordinates of the optical H II regions can be offset from the radio ones.

For every source, we give the size, systemic velocity, mean spectral index, and expansion/internal motion velocity from Hα and SGPS radio data cubes. To characterise the optical H II regions, we also used the *Spitzer*/GLIMPSE 8 μm images to note the photo-dissociation region (PDR) morphology that surrounds them. In Fig. A.7, we give an overview of the stellar cluster distribution in NGC 6334 and NGC 6357, compiled by Morales et al. (2013).

Because optical H II regions are the most evolved objects in these fields, we expect them to be the main shaping agent of the surrounding interstellar medium. Consequently, H II regions allow us to follow larger scale and older star-formation history than is probed with young stellar objects census (e.g. Willis et al. 2013; Fang et al. 2012 and Povich et al. 2013).

NGC 6334: In this part, we will refer to the region position (Fig. 1) in the Galactic coordinate system. The east and west sides of the ridge will be relative to the longitude ranges $l = 351.45°-352.2°$ and $l = 350°-351°$, respectively. The structure of NGC 6334 is dominated by a well-defined molecular ridge (e.g. Russeil et al. 2013), where the most recent and most active star-formation is located, as traced by compact radio

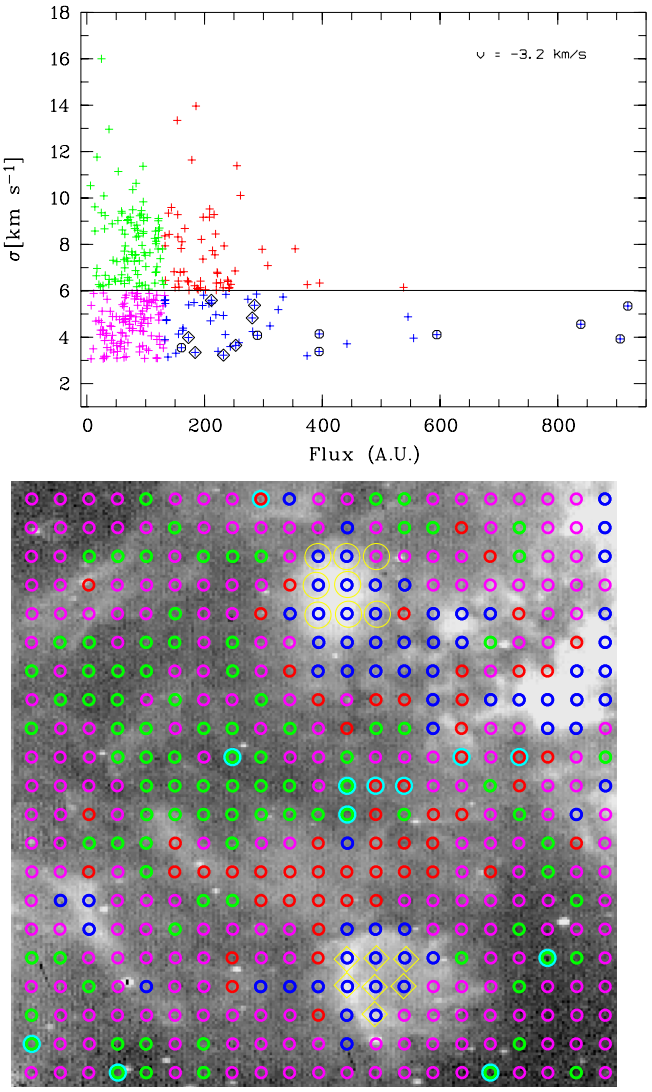

Fig. 13. Same as Fig. 10, but for the field F4 of NGC 6357. The points overlaid with lozenges and circles belong to H II 353.08+0.28 and H II 353.42+0.45, respectively. In this field, 3% of the profiles show $\sigma > 10$ km s^{-1}.

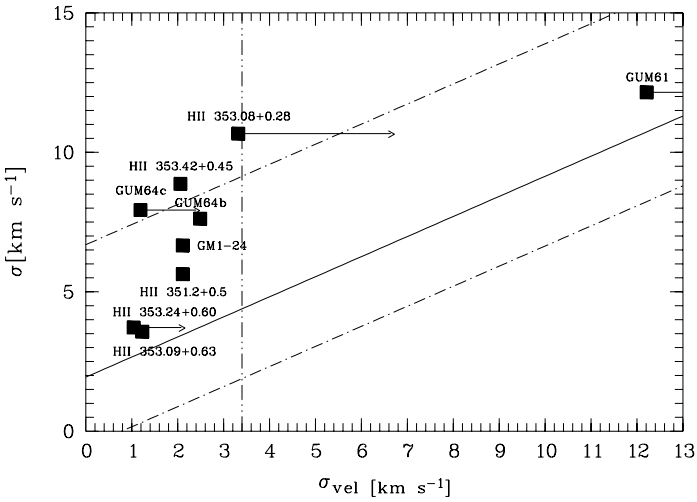

Fig. 14. The σ_{vel} versus σ diagram. The solid line indicates the linear regression (the dashed line highlight the extremes of the distribution) throught the distribution of simulated H II regions for different inclination angles from Lagrois et al. (2011) and Arthur & Hoare (2006). The vertical dash-dotted line indicates the separation between H II regions in champagne phase perturbed (on the right) or not (on the left) by an expanding wind bubble. The squares show the optical H II regions listed in Table 1. The arrows indicate the possible shift resulting from the extinction effect.

sources and young stellar clusters. The ridge is globally parallel to the Galactic plane, but at a mean latitude $b = 0.6°$. Most of the optical H II regions are located around this ridge. However, on a larger scale we note differences between the east and west sides of the ridge.

The "west side" exhibits (Fig. 1) both large and compact H II regions, as well as several thin dust/gas filaments, as defined from *Herschel* data in Russeil et al. (2013). Identified in radio, several of these large H II regions show a faint Hα counterpart.

Part of G350.710+0.642 can be observed in Hα, while it traces a large cavity at 8 μm, which is partly filled with *WISE*-22 μm emission. This cavity joins GUM 61 on its "open" side and could be impacted by its expansion.

G350.239+0.654 is also observed in Hα as a faint round (radius of ∼6.3 arcmin) H II region. At its centre there is the star LSS 4034 (Neckel 1978), whose photometric information (Reed 1998) suggests it is a B0.5 V/IV star with a distance of between 1.23 and 1.78 kpc. Small dark filaments can be seen in front of it at 8 μm, suggesting it is probably also linked to the NGC 6334 complex.

GM 1-24 appears in Hα as a north-east to south-west elongated emission made up of two diffuse bright emissions that are located on each side of the radio source G350.50+0.95 and its neighbour H II region G350.482+00.951. At 8 μm, each of these parts shows a half-ring structure that is open perpendicularly to the galactic plane, which suggests that they are two different regions that correspond to the radio regions G350.617+0.983 and G350.401+1.037, respectively. The north-east Hα emission can be associated with the cluster [DBS2003]123. Both, the radio source G350.50+0.95 and the H II region G350.482+00.951 are visible in Hα as a very compact region at velocity −10.2 km s^{-1} and −9.2 km s^{-1}, respectively, and can be associated with the clusters [DBS2003]122 and [DBS2003]121 (Morales et al. 2013), respectively. Classified by Morales et al. (2013) as a deeply embedded cluster, partially embedded cluster, and emerging-exposed cluster for [DBS2003]122, [DBS2003]121 (1.5 Myr old) ,and [DBS2003]123 (2.5 Myr old), respectively, they underscore the age gradient in this part of GM1-24. From this point of view, the formation of G350.50+0.95 may have been triggered by the interaction of these two regions.

A suggestion of triggered star-formation can also be detected on the "west side" area because compact H II regions are preferentially located at the edge and/or at the intersection of larger radio H II regions. This is the case for G350.870+0.762 and G350.889+0.728, which are found at the intersection between GUM 61 and G350.710+0.642, G350.675+0.832 (which is located at the G350.710+0.642 − G350.617+0.983 intersection) and G351.153+0.622 (a WISE compact source that is associated with a compact Hα emission for which we can determine a Hα velocity of −9.7 km s^{-1}) at the GUM 61 − HII 351.2+0.5 − NGC 6334-V intersection.

The "east side" corresponds to a cold, rather thick gas filament, as defined using *Herschel* data in Russeil et al. (2013), a group of H II regions (between $l = 351.65°$ and 351.76°) and a string of small H II regions seen at 8 μm and 22 μm (Fig. 1).

Close to the ridge, we first note two small Hα H II regions (G351.462+0.556 and G351.479+0.644) with an Hα velocity of -7 km s^{-1} and -8 km s^{-1}, respectively. They exhibit a bow-shock morphology at 70 μm (see Fig. A.5) which is similar to the bow-shock features listed by Gvaramadze et al. (2011), suggesting that they could be run-away stars coming from NGC 6334.

At ~0.3° from the ridge edge, we note a group of H II regions: G351.69+0.67, G351.68+0.61, and G351.65+0.51 and G351.766+0.492. All of them have a WISE-22 μm counterpart and are catalogued as infrared bubbles by Simpson et al. (2012). Except G351.69+0.67, all exhibit Hα counterparts and, inversely, only G351.766+0.492 is radio-quiet. At 8 μm, G351.69+0.67 is strong and has a broken bubble-like morphology, while G351.68+0.61 is a more compact radio source that probably formed at its edge. G351.65+0.51 is considered by Gvaramadze et al. (2011) as a bow-shock feature due to a run-away O8/BO III/V star that is from the cluster AH03J1726-34.4 in NGC 6357. However this group of H II regions (Fig. A.6) can be considered as an independant star-forming region since it is located along a large IR bubble (MWP1G351660+005114, Simpson et al. 2012) whose shape is underscored by a high column density feature. The radio region G351.65+0.51 itself shows a stratified dust emission with a faint PDR (traced by the 8μm emission) and an off-centred strong WISE-22 μm in spatial agreement with the Hα emission and an arc-like column-density feature.

Further away from the ridge, a string of small H II regions (G352.132+00.663, G352.060+00.636, G351.922+00.638), which can only be seen at 8 μm and 22 μm, is noted along the filament. All of them have IRAS colours, which suggests that they are probably UCHII regions (Wood & Churchwell 1989), but only G352.132+00.663 exhibits radio emission. They are catalogued as NIR-bubbles by Churchwell et al. (2009) and Simpson et al. (2012), but when not seen in Hα, they are certainly still strongly embedded. The presence of these H II regions suggests that massive star formation has already started along this cold gas/dust filament.

Finally, at about 0.33° to the north of the ridge (at $b \sim +1°$), there are G351.261+1.016 and G351.359+1.014. The region G351.261+1.016 exhibits a small but clear Hα counterpart (with velocity -11 km s^{-1}) while G351.359+1.014, bathed in the more diffuse Hα emission, is identified in radio by Langston et al. (2000). Both regions are located inside the medium scale Hα emission attributed to GUM 63. Morales et al. (2013) identify an emerging exposed cluster ([DBS2003]99) towards G351.261+1.016 that is associated with the IR-bubble CS87.

NGC 6357: The morphology of NGC 6357 is well different from NGC 6334. Its global kinematics suggests it is more turbulent than NGC 6334. In parallel, the large scale, patchy and filamentary, and kinematically complex Hα emission located to the north suggests that a previous energetic event (such as strong wind, jets or supernova) could have occurred. This is also strongly suggested by the lack of infrared counterpart.

The ionized gas is dominated by the influence of the stellar cluster Pismis 24 that hosts stars of O3 type (Massey et al. 2001), which have shaped the large cavity well known as CS 61 (Churchwell et al. 2007). Two radio sources (G353.19+0.90 and G353.19+0.84) are located on the northern edge of the cavity. G353.19+0.90 has a clear Hα counterpart while G353.19+0.84 is not optically visible and is located at the basement of the well-known fingers that face Pismis 24 (e.g. Westmoquette et al. 2012).

As already noted, four individual optical H II regions can be distinguished: H II 353.09+0.63, H II 353.24+0.60, H II 353.42+0.45, and H II 353.08+0.28. Except for H II 353.42+0.45, the three other regions exhibit a bubble or semi-bubble morphology in radio and are also listed by Churchwell et al. (2007) as CS59, CS63, and CS62 for H II 353.24+0.60, H II353.09 +0.63, and H II 353.08+0.28, respectively. Despite similar annular morphology in radio, these regions exhibit different optical and kinematic aspects. H II 353.24+0.60 has a very irregular and patchy morphology. The B2 III spectral type of the probable exciting star HD319788 (Crampton 1971) suggests that this region is more evolved. H II 353.08+0.28 exhibits a semi-ring morphology and could be wind-dominated as noted in Sect. 5.4, while H II 353.09+0.63 has a shell-like kinematic and is excited by the stellar cluster AH03J1726-34.4 (Dias et al. 2002). It also exhibits three compact radio sources on its edge that could have been triggered by its expansion. Inversely, H II 353.42+0.45 has a regular morphology and a radio spectral index that is in agreement with thermal emission. The exciting star of this region has been identified by Gvaramadze et al. (2011) as a run-away star that was expelled from the cluster AH03J1726-34.4.

Two other regions, G353.308+0.069 and G353.160+1.042, are classified by Gvaramadze et al. (2011) as run-away stars. G353.308+0.069 is identified by Gvaramadze et al. (2011) as a run-away star that has been expelled from the cluster Pismis 24. Its Hα velocity of -6 km s^{-1} confirms that it belongs to NGC 6357. G353.160+1.042 corresponds to a strong Hα emission with velocity of -11 km s^{-1}. It has a faint but clear slightly extended radio counterpart. Because it is located within a strong, larger scale Hα emission, it is difficult to distinguish it, but at 8 μm a faint rim and few small filaments surrounding a compact source can be detected, as displayed in Fig. 11 of Gvaramadze et al. (2011).

The final noticeable Hα features are the medium-scale filaments seen in Fig. 3 (Fields F4 and F2). Assuming they trace a circular morphology, they may delineate a large circular structure of 30 arcmin diameter centred on l, b = 353.343°, +0.288° (17h27m38s, −34°23′31″), but with no infrared counterpart it could be an old and diluted supernova remnant. From this perspective, the regions H II 353.42+0.45 and H II 353.08+0.28 would be located on its edge, which suggests a possible link.

7. Conclusions and perspectives

Combining multiwavelength information with Hα kinematics, we obtained the following results:

1. We clarified the nature of the radio sources, showing that they are thermal H II regions or compact H II regions with possible interacting wind. In particular, the compact radio sources located along the NGC 6334 cold dust ridge exhibit a negative spectral index, which can be interpreted as being due to colliding wind interaction.
2. We determined the nature of the optical H II regions: GUM 61 is an expanding shell-like H II region, GUM 64b exhibits a champagne flow, GM1-24 seems to be the Hα counterpart of two larger regions, H II 351.2+0.5 is in fact composed of two H II regions, H II 353.08+0.28 and H II 353.09+0.63 are probably also wind-bubble H II regions, and finally H II 353.42+0.45 is a classic H II region.
3. Thanks to their bow-shock features, two new probable running away stars were detected towards the north-east end of the NGC 6334 ridge. We anticipate that ESA-*Gaia* observations will help us to clarify the motion of these stars.

Table 1. Characteristics of the regions in NGC 6334 and NGC 6357.

Radio Ident.	Size "×"	V_{exp} km s^{-1}	V_{sys}[a] km s^{-1}	SpI[a]	Region[a]	σ_{vel} km s^{-1}	σ km s^{-1}	8 μm features[a]
			NGC 6357					
G353.43+0.46	3.0 × 3.17	1.6	−5	+0.9 (+0.49)	H II 353.42+0.45	2.06	8.87	Faint emission, rims, nascent pillars
G353.27+0.59	5.83 × 5.67	≥5	2.5	+0.3	H II 353.24+0.60	1.04	3.72	Strong emission, broken ring, pillars, known as CS59[h]
G353.19+0.90	1.83 × 2.00	16.6	−4.7	−0.5 (−0.05)	–	–	–	Semi-ring emanating from the bright rim facing Pismis 24
G353.19+0.84	0.58 × 0.67	1.2	−14.5	−0.4	–	–	–	Pillar, nascent pillar and birght rims
G353.13+0.65[b]	0.73 × 1.40	–	−4	−0.8	–	–	–	Thin and patchy filaments, at the edge of G353.08+0.63
G353.10+0.60[b]	0.75 × 0.66	–	−4	+0.8	–	–	–	no 8 μm
G353.09+0.66[b]	1.25 × 0.83	–	−4	−0.4	–	–	–	Thin and patchy filaments, edge of G353.08+0.63
G353.08+0.63[b]	4.50 × 4.33	18	−4	+0.3	H II 353.09+0.63	1.23	3.57	Strong emission, group of bubbles, pillars, known as CS63[h]
G353.07+0.31	5.32 × 6.32	8	−3	+0.6/−0.4 (+0.06)	H II 353.08+0.28	3.32	10.67	Semi-ring, pillars, rims, associated to CS62[h]
			NGC 6334					
G351.69+0.67	1.83 × 1.83	–	3.1	+1.2		–	–	Semi-ring, nascent pillar, known as CS78[h]
G351.68+0.61	1.54 × 1.54	–	–	-0.7	H II 351.67+0.62[f]	–	–	Diffuse emission with no structure
G351.65+0.51	2.83 × 2.83	–	−2.9	+0.7	H II 351.64+0.51[f]	–	–	Closed floculent ring, known as CS79[h]
G351.42+0.67	0.54 × 0.50	–	−8	−0.8	NGC 6334-E	–	–	Compact patchy emission
G351.41+0.64	0.34 × 0.34	–	−6.9	–	NGC 6334-I	–	–	Compact patchy emission
G351.38+0.74	1.83 × 1.50	17.7	−3.6	−0.4	GUM 64c	–	–	Irregular emission
G351.36+1.01[d]	1.98 × 3.40	–	−8.6	(1.06)	–	–	–	
G351.36+0.65	1.18 × 1.00	14	−5	−0.7	NGC 6334-D	–	–	Filled ring, known as CS85[h]
G351.33+0.61	0.33 × 0.33	–	−6	−0.08	NGC 6334-DS	–	–	Semi-ring, central compact source
G351.32+0.73	1.17 × 1.00	–	−8	−0.5 (−0.52)	GUM 64c	1.19	7.93	Group of 3 pillars
	6.19 × 5.53	≥6	−5	–	GUM 64b (351.32+0.61)	2.49	7.62	Irregular emission, include the small closed ring CS85[h]
G351.31+0.66	0.82 × 0.63	14	−8	−0.3	–	–	–	Core-halo feature
G351.27+0.67	0.30 × 0.30	–	–	–	–	–	–	Semi-ring feature
G351.26+1.02[d]	2.67 × 1.90	–	−3.6	–	–	–	–	Closed ring, known as CS87[h]
G351.24+0.66	0.99 × 0.42	15.7	−0.2	−1.2	NGC 6334-A	–	–	Bipolar morphology, known as CS88[h]
G351.17+0.70	1.95 × 2.19	16.5	−7	−0.9	GUM 64a	–	–	Irregular, brigth rim, known as CS89[h]
G351.15+0.49	4.43×4.37	10	−10	+0.06[c] (+0.85)	H II 351.2+0.5=GUM 62	2.11	5.63	Faint diffuse broken ring, brigth rim, include the closed ring CS90[h]
G350.99+0.65	6.06 × 4.31	23	−9	−0.6 (+1.97)	GUM 61	12.21	12.15	Broken ring, strong emission, brigth rims, known as CS94[h]
G350.50+0.95[e]	1.32 × 0.90	6.6	−10	−0.7/+0.3[e] (−0.60)	GM 1-24	2.11	6.66	

Notes. [(a)] The V_{sys} is either the radio-recombination line (Anderson et al. 2011; Caswell & Haynes 1987) or the Hα velocity. Column 5 gives the mean spectral index. The spectral index calculated between 8.35 GHz and 14.35 GHz by Langston et al. (2000) is given into parenthesis. Column 6 gives the other region's name and/or the galactic coordinates of the optical counterpart of the radio region. Column 11 gives 8 μm notes for optical H II regions only. [(b)] The regions G353.13+0.65, G353.10+0.60 and G353.09+0.66 are compact radio sources on the border of the larger and optically visible region G353.08+0.63. [(c)] This region exhibits a spectral index varying from −1 to +1 from place to place. [(d)] Radio sources not identified on radio maps but taken from Anderson et al. (2011). [(e)] G350.50+0.95 is a compact radio source located inside GM1-24 which is the more extended Hα emission. The spectral index is negative towards the compact radio source but positive in the more diffuse part of the region. [(f)] These regions are seen in Hα but they have not been observed with the Fabry-Perot interferometer. [(h)] From Churchwell et al. 2007 catalog.

4. NGC 6357 shows a more complex kinematics than NGC 6334. Conversely, NGC 6334 shows more active star-formation (as traced by the numerous compact H II regions we can detect) than NGC 6357.

The next step is to compare our results with the distribution and the characteristics of the dense and massive cores/clumps that have been detected in the sub-millimetre and far-infrared from the ATLASGAL (Schuller et al. 2009) and *Herschel*-HOBYS (Motte et al. 2010) surveys (e.g. Tigé et al., in prep.).

Acknowledgements. This study was supported by the grant ANR-TUMSE (Agence Nationale de la Recherche).

References

Anderson, L. D., Bania, T. M., Balser, D. S., et al. 2011, ApJS, 194, 32
Anderson, L. D., Bania, T. M., Balser, D. S., et al. 2014, ApJS, 212, 1
Arsenault, R., & Roy, J. R. 1988, A&A, 201, 199
Arthur S. J., & Hoare, M. G. 2006, ApJS, 165, 283
Benaglia, P., Romero, G. E., Koribalski, B., & Pollock, A. M. T. 2005, A&A, 440, 743
Bitran, M., Alvarez, H., Bronfman, L., et al. 1997, A&AS, 125, 99
Blasco-Herrera, J., Fathi, K., Beckman, J., et al. 2010, MNRAS, 407, 2519
Bodenheimer, P.,Tenorio-Tagle, G., & Yorke H. M. 1979, ApJ, 233, 85
Bohigas, J., Tapia, M., Roth, M., et al. 2004, AJ, 127, 2826
Bohlin, R. C., Savage, B. D., & Drake, J. F. 1978, ApJ, 224, 132
Brand, J., Massi, F., Zavagno, A., et al. 2011, A&A, 527, A62
Brooks, K. J., & Whiteoak, J. B. 2001, MNRAS, 320, 465
Cappa, C. E., Barbá, R., Duronea, N. U., et al. 2011, MNRAS, 415, 2844
Carral, P., Kurtz, S. E., Rodríguez, L. F., et al. 2002, AJ, 123, 2574
Caswell, J. L., & Haynes, R. F. 1987, A&A, 171, 261
Churchwell, E., Watson, D. F., Povich, M. S., et al. 2007, ApJ, 670, 428
Churchwell, E., Babler, B. L., Meade, M. R., et al. 2009, PASP, 121, 213
Crampton, D. 1971, AJ, 76, 260
Cohen, M., Green, A. J., Meade, M. R., et al. 2007, MNRAS, 374, 979
Comeron, F. 1997, A&A, 326, 1195
Dame, T. M., Ungerechts, H., Cohen, R. S., et al. 1987, ApJ, 322, 706
Deharveng, L., Schuller, F., Anderson, L. D., et al. 2010, A&A, 523, A6
Dias, W., Alessi, B., Moitinho, A., et al. 2002, A&A, 389, 871
Dutra, C. M., & Bica, E. 2002, A&A, 383, 631
Emprechtinger, M., Lis, D. C., Bell, T., et al. 2010, A&A, 521, L28
Emprechtinger, M., Lis, D. C., Rolffs, R., et al. 2013, ApJ, 765, 61
Fang M., van Boeckel, R., King, R. R., et al. 2012, A&A, 539, A119
Foster, T., & MacWilliams, J. 2006, ApJ, 644, 214
Georgelin, Y. M., Amram, P., Georgelin, Y. P., et al. 1994, A&AS, 108, 513
Green, A. J., Cram, L. E., Large, M. I., et al. 1999, ApJS, 122, 207
Green, D. A. 2006, A Catalogue of Galactic Supernova Remnants (Cambridge: Cavendish Lab.), http://www.mrao.cam.ac.uk/surveys/snrs/
Gvaramadze, V. V., Kniazev, A. Y., Kroupa P., et al. 2011, A&A, 535, A29
Haverkorn, M., Gaensler, B. M., McClure-Griffiths, N. M., et al. 2006, ApJS, 167, 230
Johnson, H. M. 1982, ApJ, 256, 559
Kraemer, K. E., & Jackson, J. M. 1999, ApJS, 124, 439
Lagrois, D., Joncas, G., Drissen, L., et al. 2011, MNRAS, 413, 705
Langston, G., Minter, A., D'addario L., et al. 2000, AJ, 119, 2801
Le Coarer, E., Amram, P., Boulesteix, J., et al. 1992, A&A, 257, 389
Lima, E. F., Bica, E., Bonatto, C., & Saito, R. K. 2014, A&A, 568, A16
Lortet, M. C., Testor, G., & Niemela, V. 1984, A&A, 140, 24
Luque-Escamilla, P. L., Muñoz-Arjonilla, A. J., Sánchez-Sutil, J. R., et al. 2011, A&A, 532, A92
van Marle, A. J., & Keppens, R. 2012, A&A, 547, A3
Massey, P., DeGioia-Eastwood, K., & Waterhouse, E. 2001, AJ, 121, 1050
Massi, F., Brand, J., & Felli, M. 1997, A&A, 320, 972
McClure-Griffiths, N. M., Dickey, J. M., Gaensler, B. M., et al. 2005, ApJS, 158, 178
Minter, A. 2008, ApJ, 677, 373
Moiseev, A., & Lozinskaya, T. 2012, MNRAS, 423, 1831
Morales, E. F. E., Wyrowski, F., Schuller F., et al. 2013, A&A, 560, A76
Motte, F., Zavagno, A., Bontemps, S., et al. 2010, A&A, 518, L77
Muñoz, D., Mardones, D., Garay, G., et al. 2007, ApJ, 668, 906
Muñoz-Tuñón, C., Tenorio-Tagle, G., Castañeda, H., et al. 1996, AJ, 112, 1636
Neckel, T. 1978, A&A, 69, 51
Nelder, J. A., & Mead, R. 1965, Comp. J., 7, 308
O'Dell C. R., & Townsley L. K. 1988, A&A, 198, 283
Otrupcek, R. E., Hartley, M., & Wang, J.-S. 2000, PASA, 17, 92
Parker, Q. A. P., Philipps, S., Pierce, M., et al. 2005, MNRAS, 362, 689
Persi, P., & Tapia, M. 2008, Handbook of Star Forming Regions, Vol. II: The Southern Sky ASP Monograph Publications, Vol. 5. eds. Bo Reipurth, 456
Povich, M. S., Kuhn, M. A., Getman, K. V., et al. 2013, ApJS, 209, 31
Radhakrishnan, V., Goss, W. M., Murray J. D., et al. 1972, ApJSS, 203, 49
Reich, P., & Reich, W. 1988, A&AS, 74, 7
Reed, B. C. 1998, ApJS, 115, 271
Relaño, M., Beckman, J., Zurita, A., et al. 2005, A&A, 431, 235
Reynolds, S. P. 1986, ApJ, 304, 713
Robinson, B. J., Manchester, R. N., Whiteoak, J. B., et al. 1988, A&A, 193, 60
Rodríguez, L. F., Masqué, J. M., Dzib, S. A., et al. 2014, Rev. Mex. Astron. Astrofis., 50, 3
Rozas, M., Richer, M. G., López, J. A., et al. 2006, A&A, 455, 549
Russeil, D., Adami, C., Amram, P., et al. 2005, A&A, 429, 497
Russeil, D., Zavagno, A., Motte, F., et al. 2010, A&A, 515, A55
Russeil, D., Zavagno, A., Adami, C., et al. 2012, A&A, 538, A142
Russeil, D., Schneider, N., Anderson, L. D., et al. 2013, A&A, 554, A42
Sana H., Le Bouquin J. B., Lacour S., et al. 2014, ApJS, 215, 15
Schraml, J., & Mezger, P. G. 1969, ApJ, 156, 269
Schuller, F., Menten, K. M., Contreras, Y., et al. 2009, A&A, 504, 415
Simpson, R. J., Povich, M. S., Kendrew, S., et al. 2012, MNRAS, 424, 2442
Sota A., Mainz Apellaniz J., Morrell N. I., et al. 2014, ApJS, 211, 10
Strasser, S. T., Dickey, J. M., Taylor, A. R., et al. 2007, AJ, 134, 2252
Tapia, M., Persi, P., & Roth, M. 1996, A&A, 316, 102
Tenorio-Tagle, G. 1979, A&A, 71, 59
Thompson, M. A., Urquhart, J. S., Moore, T. J., et al. 2012, MNRAS, 421, 408
Tian, W. W., Haverkorn, M., & Zhang, H. Y. 2007, MNRAS, 378, 1283
Townsley, L. K., Broos, P. S., Gordon P. G., et al. 2014, ApJS, 213, 1
Tremblin, P., Audit, E., Minier, V., et al. 2012a, A&A, 538, A31
Tremblin, P., Audit, E., Minier, V., et al. 2012b, A&A, 546, A33
van der Wiel, M. H. D., van der Tak, F. F. S., Lis, D. C., et al. 2010, A&A, 521, L5
Walsh A. J., Breen, S. L., Britton, T., et al. 2011, MNRAS, 416, 1764
Westmoquette, M. S., Slavin, J. D., Smith, L. J., et al. 2010, MNRAS, 402, 152
Westmoquette, M. S., Dale, J. E., Ercolano, B., & Smith, L. J. 2013, MNRAS, 435, 30
Willis, S., Marengo, M., Allen, L., et al. 2013, ApJ, 778, 96
Wood, D. O. S., & Churchwell, E. 1989, ApJ, 340, 265
Zavagno, A., Russeil, D., Motte, F., et al. 2010a, A&A, 518, L81
Zavagno, A., Anderson, L. D., & Russeil, D. 2010b, A&A, 518, L101
Zernickel, A., Schilke, P., Schmiedeke, A., et al. 2012, A&A, 546, A87

Appendix A: Additionnal figures and tables

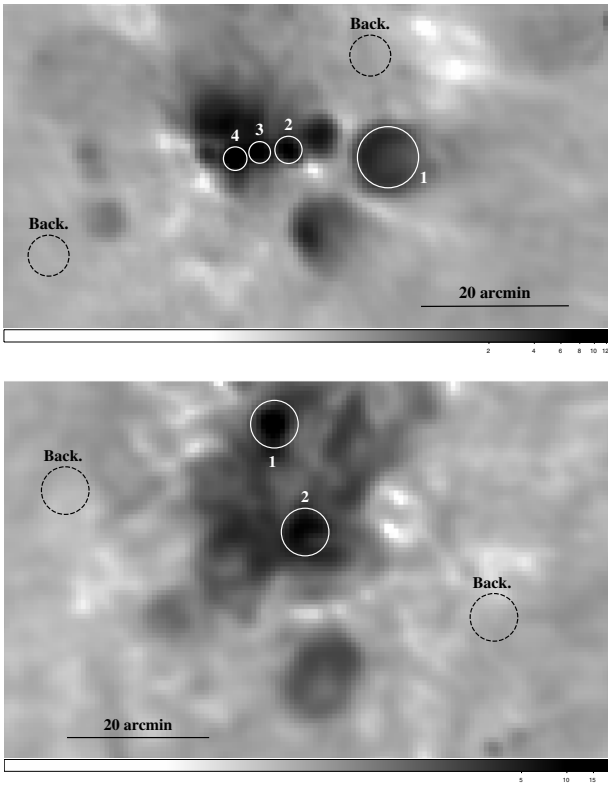

Fig. A.1. HI continuum images (in Jy/beam) of NGC 6334 (*up*) and NGC 6357 (*down*). The background and "on source" areas (identification number) are indicated.

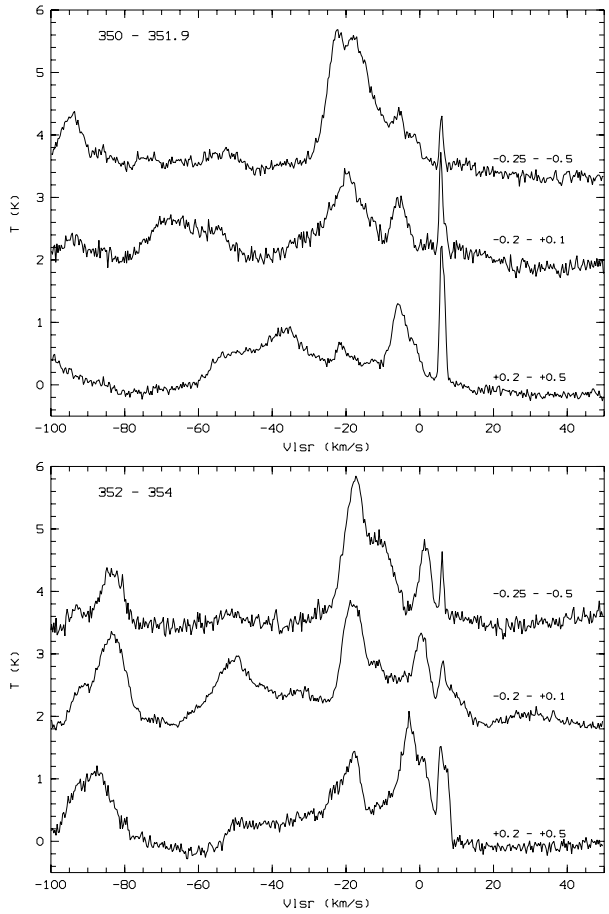

Fig. A.2. ^{12}CO average profiles extracted from ThrUMMS data cubes. The profiles are averaged over $b = -0.25°$ to $-0.5°$ (*top*), $b = -0.2°$ to $+0.1°$ (*middle*) and $b = 0.2°$ to $0.5°$ (*bottom*) and $l = 350°$ to $351.9°$ and $l = 352°$ to $354°$, respectively. The profiles are vertically-shifted from each other to better compare them.

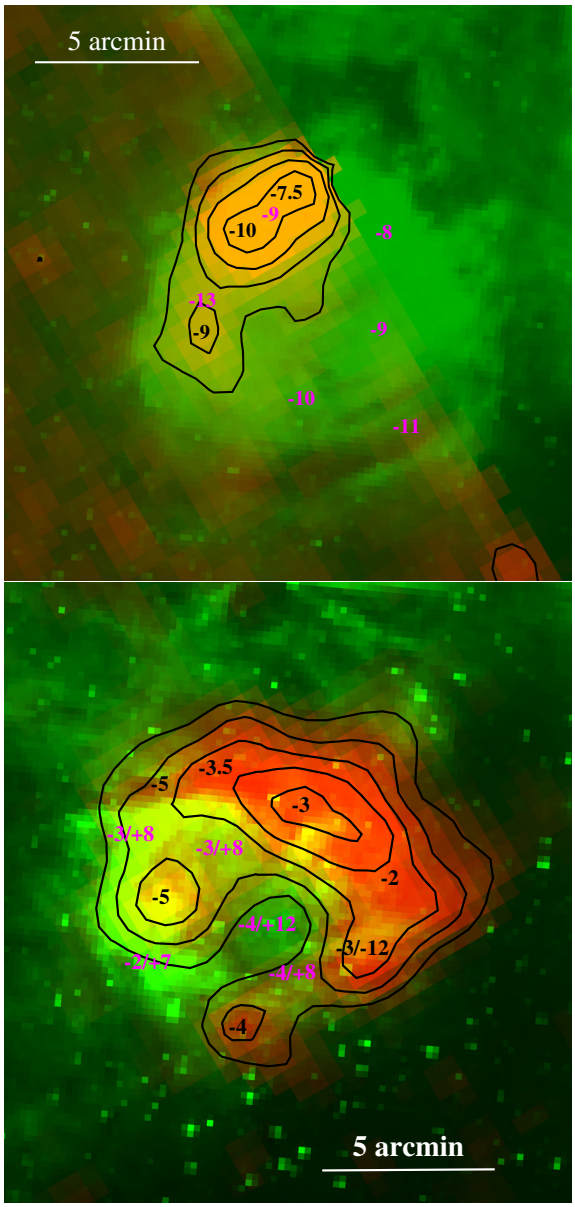

Fig. A.3. Hα (green) and H69α (red) composite image (North up, East left) of HII 351.2+0.5 (*upper panel*) and G353.08+0.28 (*lower panel*). The black and magenta numbers gives the radio line and the optical Hα line velocity, respectively. Note that G351.2+0.5 is only partly covered by the HOPS survey.

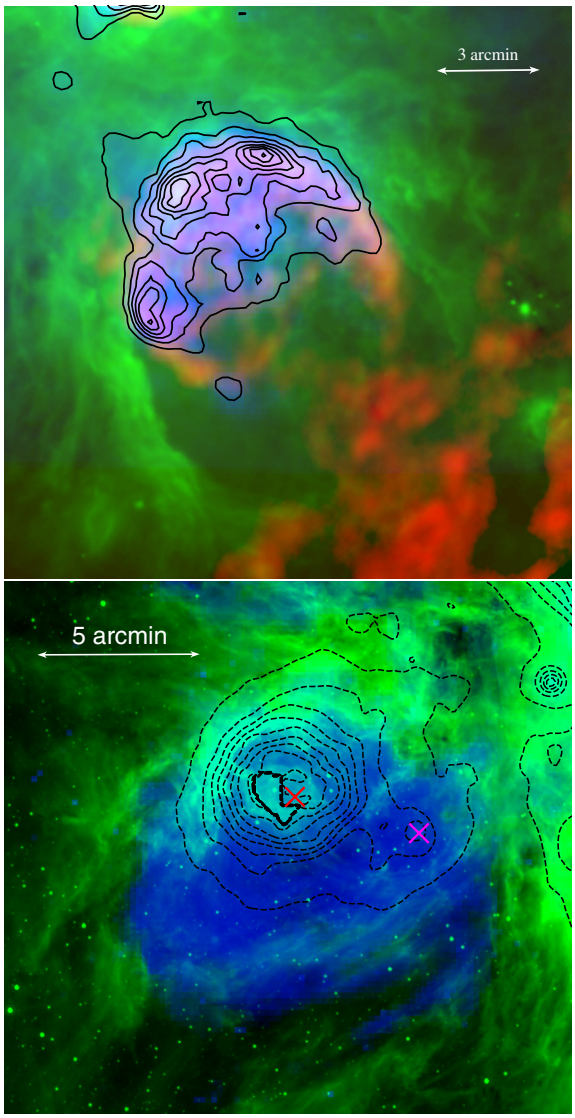

Fig. A.4. Composite image (North up, East left) of GUM 61 (*upper panel*) and H II351.2+0.5 (*lower panel*). *In the upper panel*, the RGB colors are: ATCA continuum 1.6 GHz (Munõz et al. 2007), *Hershel* – 70 μm (Russeil et al. 2013), and UKST Hα (Parker et al. 2005), enhanced with isocontours. *In the lower panel* the colours are: *Spitzer* – 8 μm in green and UKST Hα (Parker et al. 2005) in blue. The isocontours trace the *WISE*-22 μm emission (the final isocontour underlines the saturated area). The red and magenta crosses indicate the stars HD156738 and ALS 4095, respectively (see text).

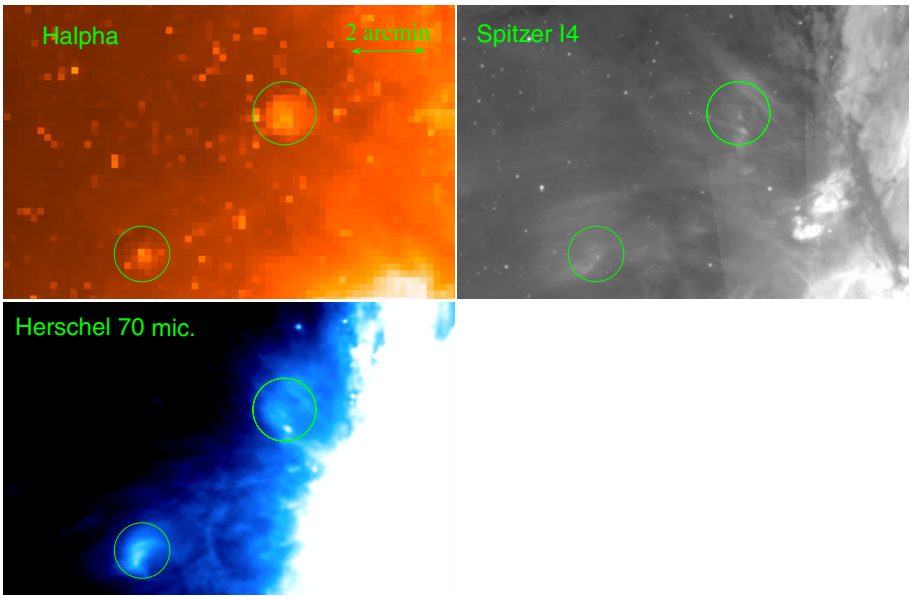

Fig. A.5. Bow-shock features around G351.462+0.556 and G351.479+0.644. *Spitzer*-I4 image is the 8 μm image.

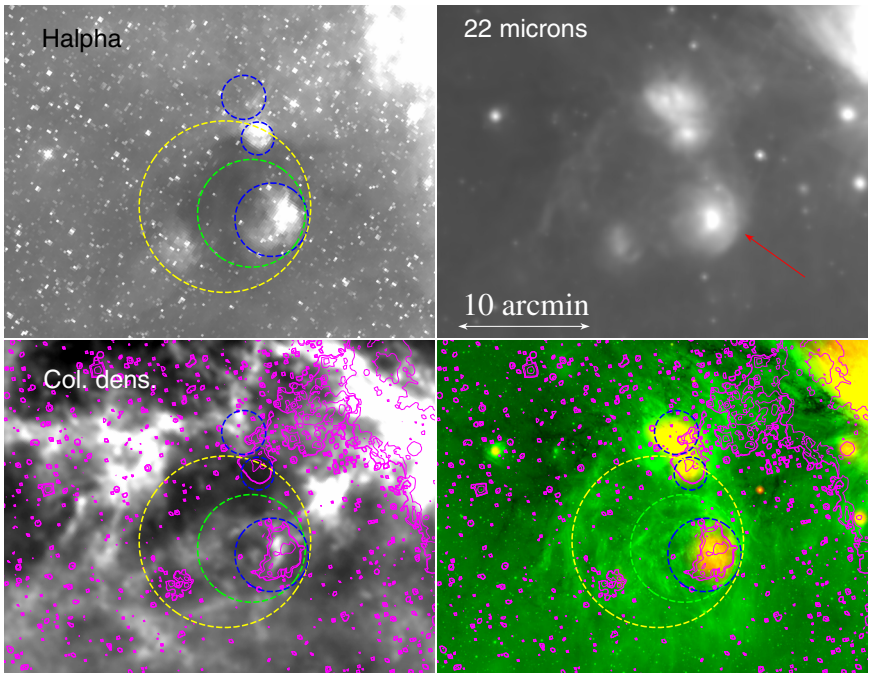

Fig. A.6. Multiwavelength view (galactic coordinates orientation) of the group of H II regions (G351.65+0.51, G351.69+0.67, G351.68+0.61, and G351.766+0.492). Blue dashed circles indicate the radio sources while the green and yellow circles underline the 8 μm bubbles. *The lower-right image* combines *Spitzer*-8 μm (green) and WISE-22 μm (red) images. The magenta isocontours underline the Hα emission. Similar to Gvaramadze et al. (2011), the bow-shock aspect of G351.65+0.51 can be seen on the WISE-22 μm image (red arrow in the *upper-right panel*).

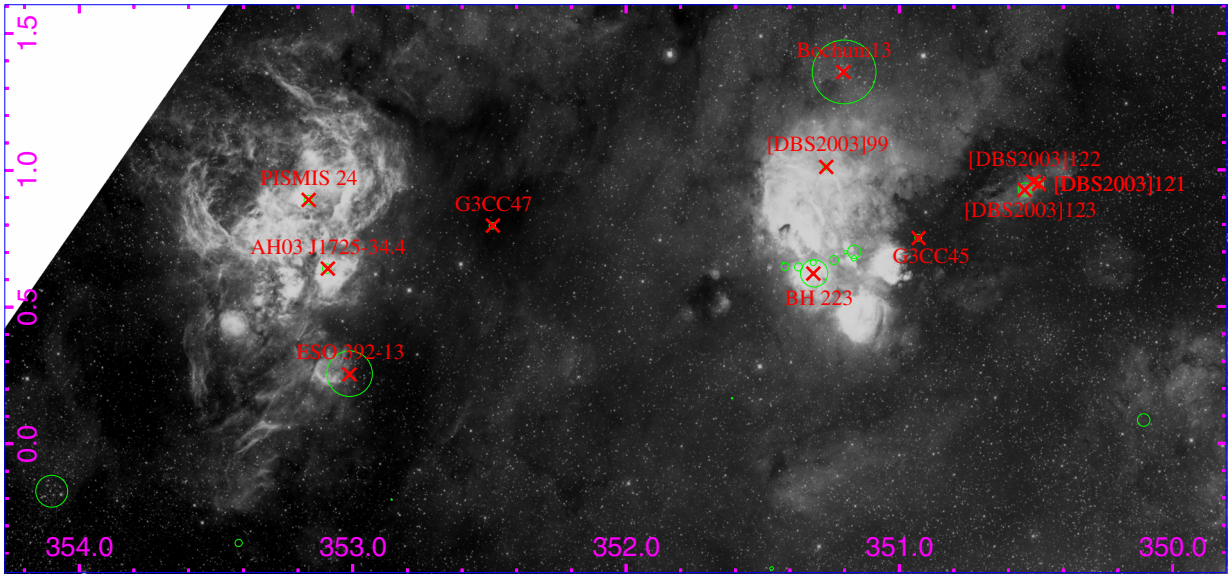

Fig. A.7. AAO-UKST Hα image of NGC 6334 and NGC 6357. The clusters listed by Morales et al. (2013) are overlaid (green circles). For most of them their name is indicated in red.

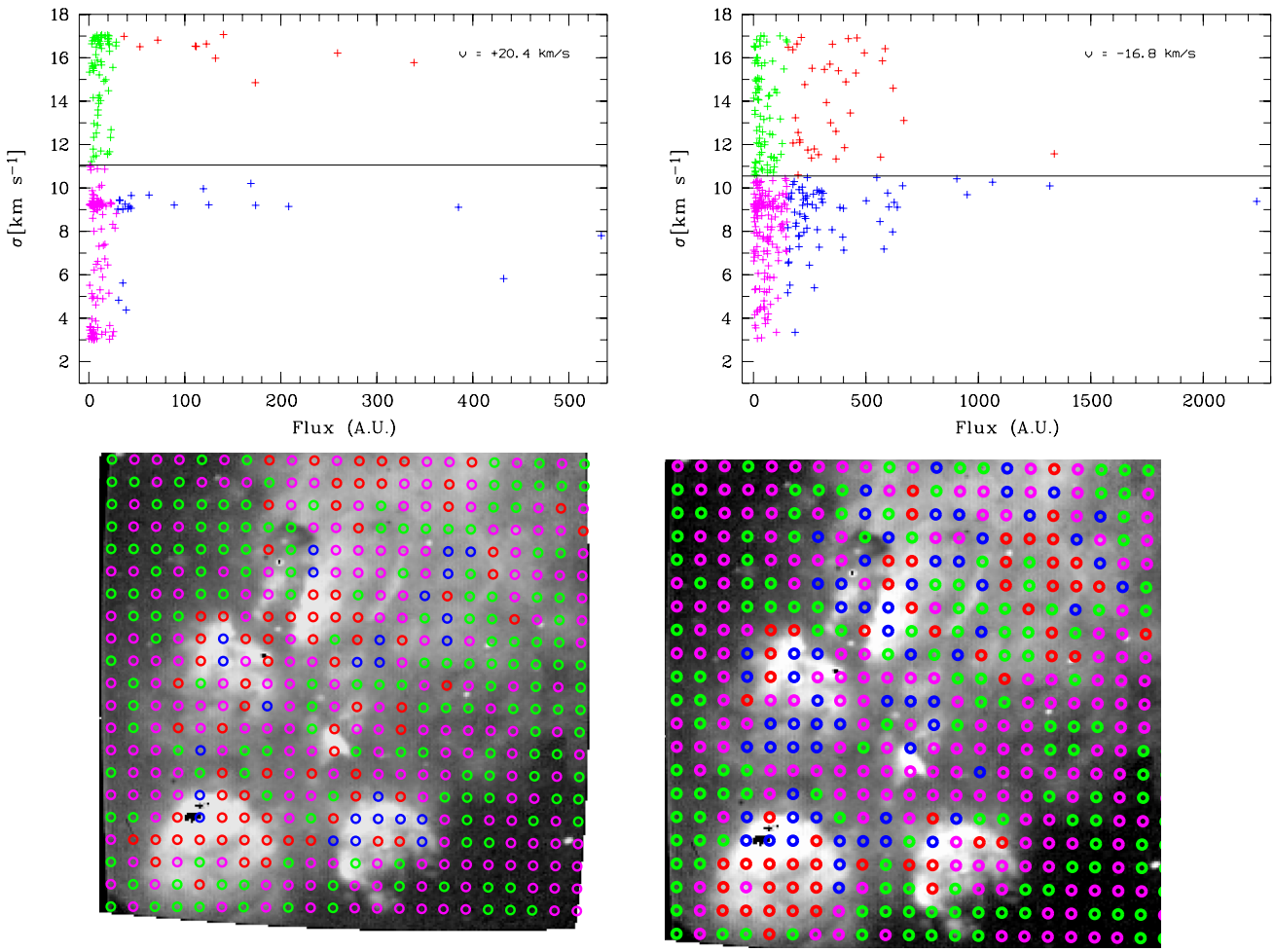

Fig. A.8. Same as for Fig. 10 for the two other fitted components.

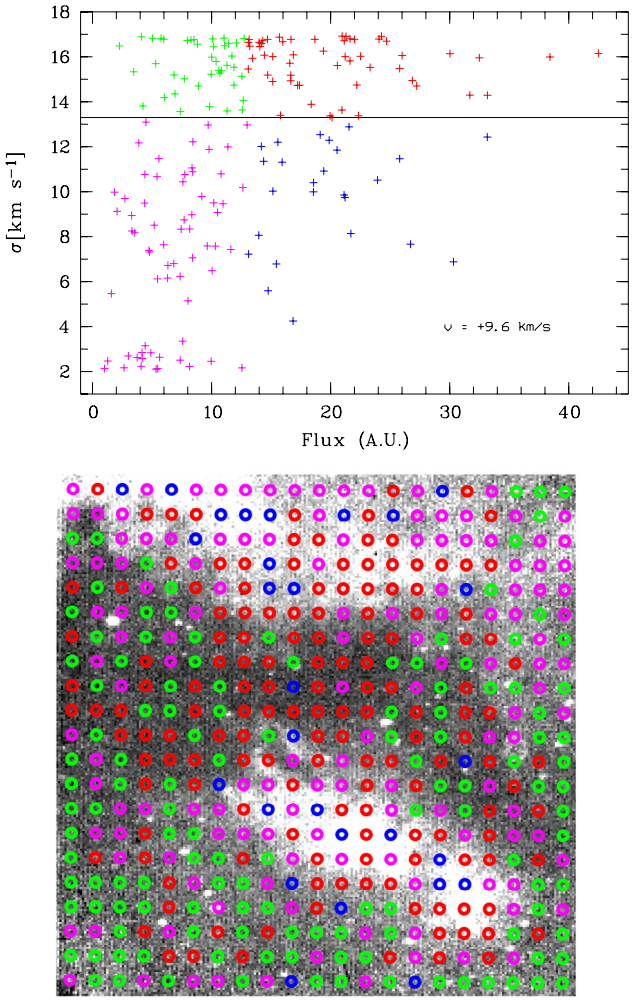

Fig. A.9. Same as for Fig. 11 for the other fitted component.

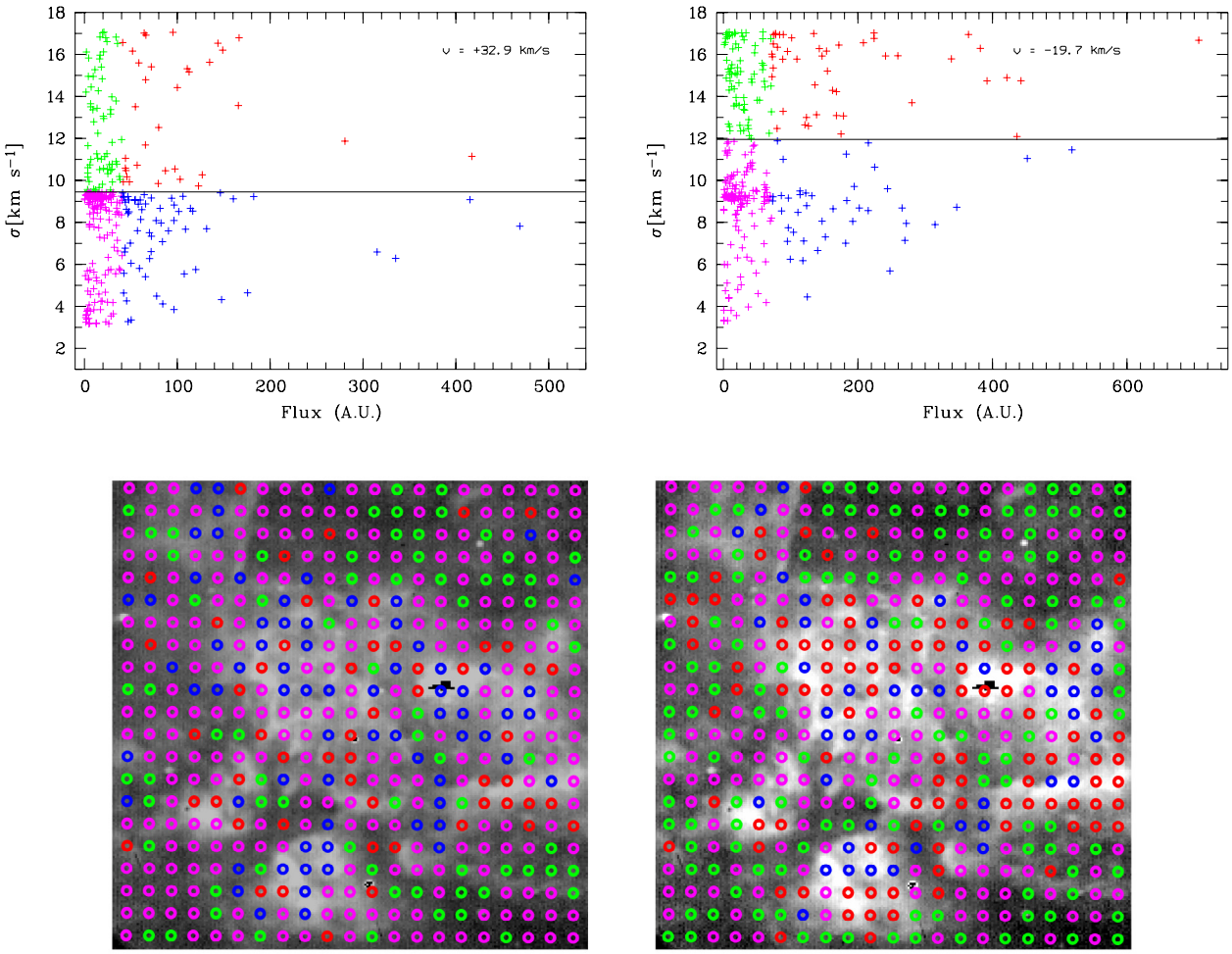

Fig. A.10. Same as for Fig.12 for the two other fitted components.

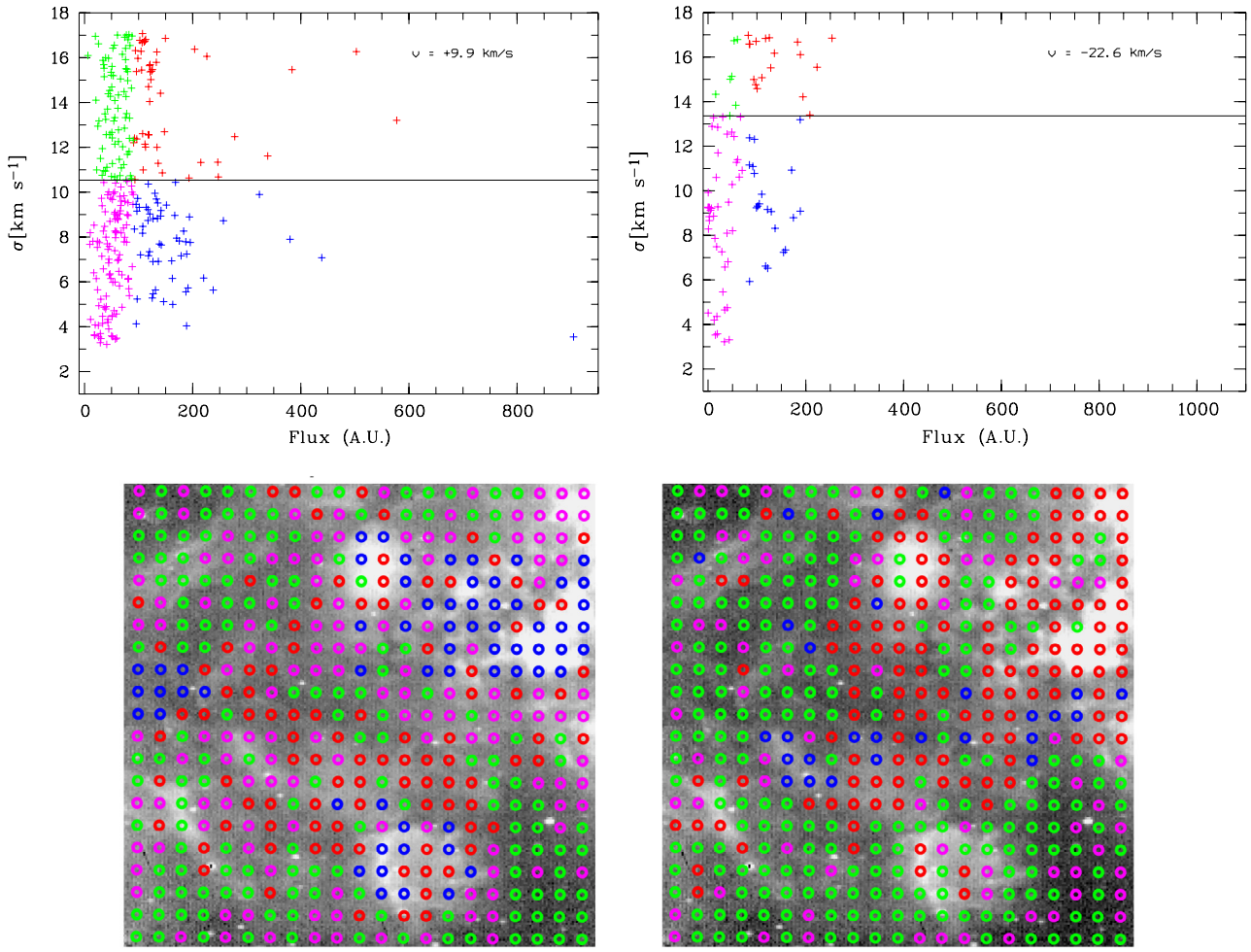

Fig. A.11. Same as for Fig. 13 for the two other fitted components.

Table A.1. Langston et al. (2000) and Anderson et al. (2014) H II regions in NGC 6334 and NGC 6357.

Langston et al. GPA Ident.	Anderson et al. HRDS Ident.	Hα/H II region association
	NGC 6357	
352.87+1.21	352.794+1.360	Hα?
352.95+0.93	352.838+0.934	Hα
–	353.037+0.452	Hα?
–	353.048+0.553	H II 353.09+0.63
–	353.063+0.529	H II 353.09+0.63
–	353.088+0.449	
–	353.091+0.857	pismis 24
353.10+0.35	353.0762+0.287	H II 353.08+0.28
–	353.160+1.042	Hα
353.19+0.67	353.272+0.591 + 353.037 0.581	H II 353.24+0.60
353.20+0.92	353.194+0.910	Hα
353.24+1.04	353.235+1.060	Hα
353.37+0.74	–	Hα
–	353.308+0.069	Hα
–	353.383+0.430	H II 353.43+0.44
353.42+0.45	353.435+0.426	H II 353.43+0.44
–	353.452+0.324	
353.58+0.86	–	Hα?
	NGC 6334	
–	350.239+0.654	Hα
–	350.401+1.037	GM1-24
–	350.482+0.951	compact Hα in GM1-24
–	350.505+0.956	compact Hα in GM1-24
350.59+0.97	350.617+0.983	GM1-24
–	350.675+0.832	Hα
–	350.706+0.998	
–	350.715+1.044	
350.77+0.68	350.710+0.642	Hα
–	350.870+0.762	
–	350.889+0.728	
–	350.958+0.358	Hα
350.99+0.67	350.994+0.654	GUM 61
–	351.016+0.856	GUM 63
351.06+0.98	–	GUM 63
–	351.094+0.799	GUM 63
–	351.153+0.622	Hα
–	351.169+0.703	GUM 63
351.21+0.44	351.129+0.449	H II 351.2+0.5
–	351.246+0.673	GUM 63
–	351.261+1.016	GUM 63
–	351.311+0.663	GUM 63
351.34+0.71	–	GUM 63
–	351.348+0.592	GUM 63
351.36+1.01	351.359+1.014	GUM 63
–	351.367+0.640	GUM 63
351.39+0.74	351.382+0.737	GUM 64c
–	351.420+0.638	GUM 63
–	351.423+0.650	Hα
–	351.462+0.556	Hα
–	351.479+0.644	Hα
–	351.650+0.510	Hα
–	351.676+0.610	Hα
–	351.692+0.671	
–	351.766+0.492	Hα
–	351.834+0.756	